2. Nanomaterials Synthesis and Applications: Molecule-Based Devices

Françisco M. Raymo

The constituent components of conventional devices are carved out of larger materials relying on physical methods. This top-down approach to engineered building blocks becomes increasingly challenging as the dimensions of the target structures approach the nanoscale. Nature, on the other hand, relies on chemical strategies to assemble nanoscaled biomolecules. Small molecular building blocks are joined to produce nanostructures with defined geometries and specific functions. It is becoming apparent that nature's bottom-up approach to functional nanostructures can be mimicked to produce artificial molecules with nanoscaled dimensions and engineered properties. Indeed, examples of artificial nanohelices, nanotubes, and molecular motors are starting to be developed. Some of these fascinating chemical systems have intriguing electrochemical and photochemical properties that can be exploited to manipulate chemical, electrical, and optical signals at the molecular level. This tremendous opportunity has led to the development of the molecular equivalent of conventional logic gates. Simple logic operations, for example, can be reproduced with collections of molecules operating in solution. Most of these chemical systems, however, rely on bulk addressing to execute combinational and sequential logic operations. It is essential to devise methods to reproduce these useful functions in solid-state configurations and, eventually, with single molecules. These challenging objectives are stimulating the design of clever devices that interface small assemblies of organic molecules with macroscaled and nanoscaled electrodes. These strategies have already produced rudimentary examples of diodes, switches, and transistors based on functional molecular components. The rapid and continuous progress of this exploratory research will, we hope, lead to an entire generation of molecule-based devices that might ultimately find useful applications in a variety of fields, ranging from biomedical research to information technology.

2.1 Chemical Approaches to Nanostructured Materials

The fabrication of conventional devices relies on the assembly of macroscopic building blocks with specific configurations. The shapes of these components are carved out of larger materials by exploiting physical methods. This top-down approach to engineered building blocks is extremely powerful and can deliver effectively and reproducibly microscaled objects. This strategy becomes increasingly challenging, however, as the dimensions of the target structures approach the nanoscale. Indeed, the physical fabrication of nanosized features with subnanometer precision is a formidable technological challenge.

2.1.1 From Molecular Building Blocks to Nanostructures

Nature efficiently builds nanostructures by relying on chemical approaches. Tiny molecular building blocks are assembled with a remarkable degree of structural control in a variety of nanoscaled materials with defined shapes, properties, and functions. In contrast to the top-down physical methods, small components are connected to produce larger objects in these bottom-up chemical strategies. It is becoming apparent that the limitations of the top-down approach to artificial nanostructures can be overcome by mimicking nature's bottom-up processes. Indeed, we are starting to see emerge beautiful and ingenious examples of molecule-based strategies to fabricate chemically nanoscaled building blocks for functional materials and innovative devices.

2.1.2 Nanoscaled Biomolecules: Nucleic Acids and Proteins

Nanoscaled macromolecules play a fundamental role in biological processes [2.1]. Nucleic acids, for example, ensure the transmission and expression of genetic information. These particular biomolecules are linear polymers incorporating nucleotide repeating units (Fig. 2.1a). Each nucleotide has a phosphate bridge and a sugar residue. Chemical bonds between the phosphate of one nucleotide and the sugar of the next ensures the propagation of a polynucleotide strand from the 5′ to the 3′ end. Along the sequence of alternating sugar and phosphate fragments, an extended chain of robust covalent bonds involving carbon, oxygen, and phosphorous atoms forms the main backbone of the polymeric strand.

Every single nucleotide of a polynucleotide strand carries one of the four heterocyclic bases shown in Fig. 2.1b. For a strand incorporating 100 nucleotide repeating units, a total of 4^{100} unique polynucleotide sequences are possible. It follows that nature can fabricate a huge number of closely related nanostructures relying only on four building blocks. The heterocyclic bases appended to the main backbone of alternating phosphate and sugar units can sustain hydrogen bonding and $[\pi \cdots \pi]$ stacking interactions. Hydrogen bonds, formed between [N−H] donors and either N or O acceptors, encourage the pairing of adenine (A) with thymine (T) and of guanine (G) with cytosine (C). The stacking interactions involve attractive contacts between the extended π-surfaces of heterocyclic bases.

In the *B* conformation of deoxyribonucleic acid (DNA), the synergism of hydrogen bonds and $[\pi \cdots \pi]$ stacking glues pairs of complementary polynucleotide strands in fascinating double helical supermolecules (Fig. 2.1c) with precise structural control at the subnanometer level. The two polynucleotide strands wrap around a common axis to form a right-handed double helix with a diameter of ≈ 2 nm. The hydrogen bonded and $[\pi \cdots \pi]$ stacked base pairs lie at the core of the helix with their π-planes perpendicular to the main axis of the helix. The alternating phosphate and sugar units define the outer surface of the double helix. In *B*-DNA, ≈ 10 base pairs define each helical turn corresponding to a rise per turn or helical pitch of ≈ 3 nm. Considering that these molecules can incorporate up to $\approx 10^{11}$ base pairs, extended end-to-end lengths spanning from only few nanometers to hundreds of meters are possible.

Nature's operating principles to fabricate nanostructures are not limited to nucleic acids. Proteins are also built joining simple molecular building blocks, the amino acids, by strong covalent bonds [2.1]. More precisely, nature relies on 20 amino acids differing in their side chains to assemble linear polymers, called polypeptides, incorporating an extended backbone of robust [C−N] and [C−C] bonds (Fig. 2.2a). For a single polymer strand of 100 repeating amino acid units, a total of 20^{100} unique combinations of polypeptide sequences are possible. Considering that proteins can incorporate more than one polypetide chain with over 4000 amino acid residues each, it is obvious that nature can assemble an enormous number of different biomolecules relying on the same fabrication strategy and a relatively small pool of building blocks.

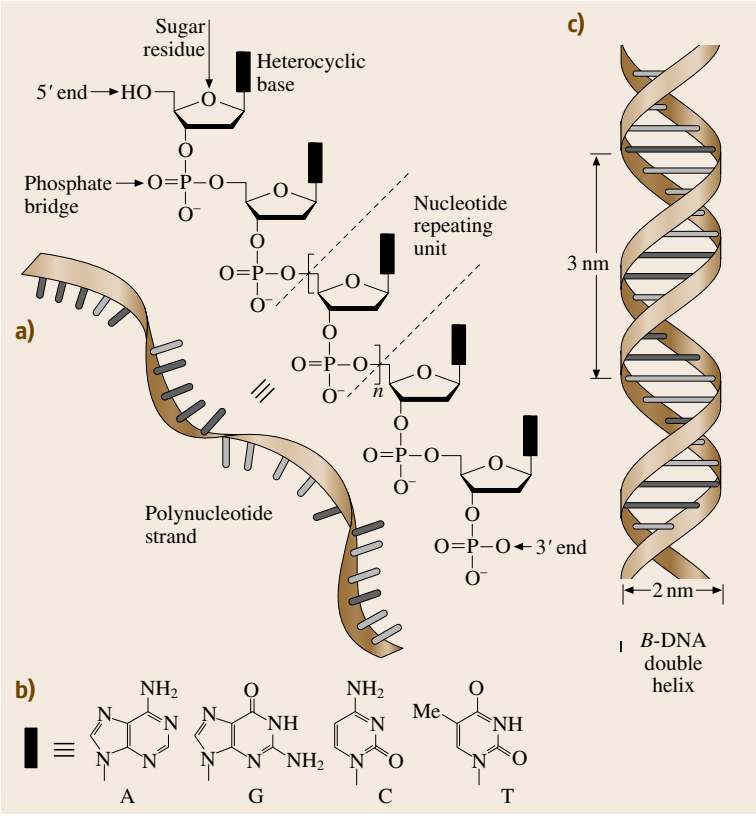

Fig. 2.1a–c A polynucleotide strand **(a)** incorporates alternating phosphate and sugar residues joined by covalent bonds. Each sugar carries one of four heterocyclic bases **(b)**. Noncovalent interactions between complementary bases in two independent polynucleotide strands encourage the formation of nanoscaled double helixes **(c)**

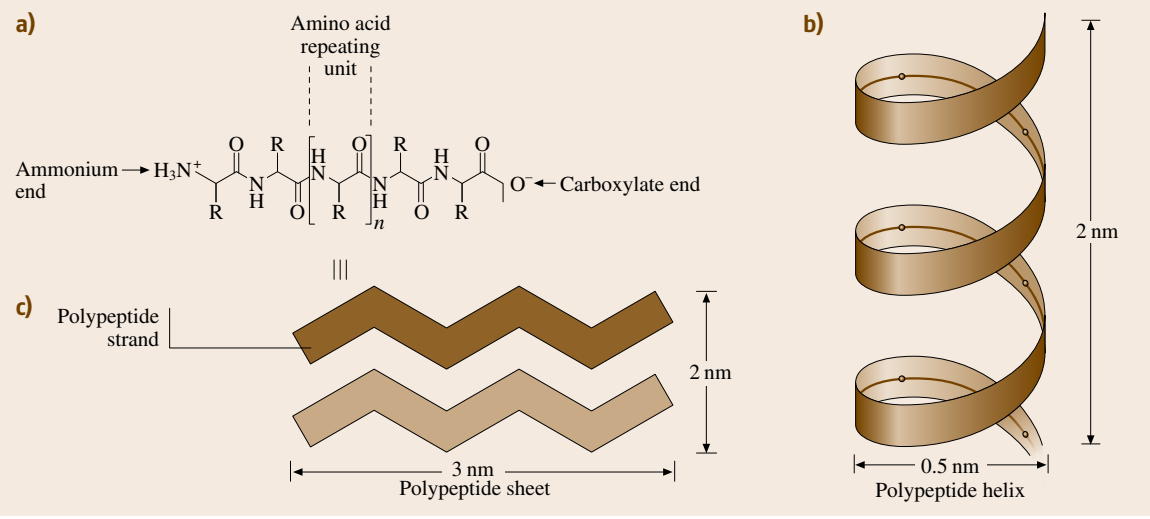

Fig. 2.2a–c A polypeptide strand **(a)** incorporates amino acid residues differing in their side chains and joined by covalent bonds. Hydrogen bonding interactions curl a single polypeptide strand into a helical arrangement **(b)** or lock pairs of strands into nanoscaled sheets **(c)**

The covalent backbones of the polypeptide strands form the main skeleton of a protein molecule. In addition, a myriad of secondary interactions, involving noncovalent contacts between portions of the amino acid residues, control the arrangement of the individual polypeptide chains. Intrastrand hydrogen bonds curl single polypeptide chains around a longitudinal axis in a helical fashion to form tubular nanostructures ≈ 0.5 nm wide and ≈ 2 nm long (Fig. 2.2b). Similarly, interstrand hydrogen bonds can align from 2 up to 15 parallel or antiparallel polypeptide chains to form nanoscaled sheets with average dimensions of 2×3 nm^2 (Fig. 2.2c). Multiple nanohelices and/or nanosheets combine into a unique three-dimensional arrangement dictating the overall shape and dimensions of a protein.

2.1.3 Chemical Synthesis of Artificial Nanostructures

Nature fabricates complex nanostructures relying on simple criteria and a relatively small pool of molecular building blocks. Robust chemical bonds join the basic components into covalent scaffolds. Noncovalent interactions determine the three-dimensional arrangement and overall shape of the resulting assemblies. The multitude of unique combinations possible for long sequences of chemically connected building blocks provides access to huge libraries of nanoscaled biomolecules.

Modern chemical synthesis has evolved considerably over the past few decades [2.2]. Experimental procedures to join molecular components with structural control at the picometer level are available. A multitude of synthetic schemes to encourage the formation of chemical bonds between selected atoms in reacting molecules have been developed. Furthermore, the tremendous progress of crystallographic and spectroscopic techniques has provided efficient and reliable tools to probe directly the structural features of artificial inorganic and organic compounds. It follows that designed molecules with engineered shapes and dimensions can be now prepared in a laboratory relying on the many tricks of chemical synthesis and the power of crystallographic and spectroscopic analyses.

The high degree of sophistication reached in this research area translates into the possibility of mimicking the strategies successfully employed by nature to fabricate chemically nanostructures [2.3]. Small molecular building blocks can be synthesized and joined covalently following routine laboratory procedures. It is even possible to design the stereoelectronic properties of the assembling components in order to shape the geometry of the final product with the assistance of noncovalent interactions. For example, five bipyridine building blocks (Fig. 2.3) can be connected in five synthetic steps to produce an oligobipyridine strand [2.4]. The five repeating units are bridged by C−O bonds and can chelate metal cations in the bay regions defined by their two nitrogen atoms. The spontaneous assembly of two organic strands in a double helical arrangement occurs in the presence of inorganic cations. In the resulting helicate, the two oligobipyridine strands wrap around an axis defined by five Cu(I) centers. Each inorganic cation coordinates two bipyridine units with a tetrahedral geometry imposing a diameter of ≈ 0.6 nm on the nanoscaled helicate [2.5]. The overall length from one end of the helicate to the other is ≈ 3 nm [2.6]. The analogy between this artificial double helix and the *B*-DNA double helix shown in Fig. 2.1c is obvious. In both instances, a supramolecular glue combines two independent molecular strands into nanostructures with defined shapes and dimensions.

The chemical synthesis of nanostructures can borrow nature's design criteria as well as its molecular building blocks. Amino acids, the basic components of proteins, can be assembled into artificial macrocycles. In the example of Fig. 2.4, eight amino acid residues are joined through the formation of C−N bonds in multiple synthetic steps [2.7]. The resulting covalent backbone defines a circular cavity with a diameter of ≈ 0.8 nm [2.8]. In analogy to the polypeptide chains of proteins, the amino acid residues of this artificial oligopeptide can sustain hydrogen bonding interactions. It follows that multiple macrocycles can pile on top of each other to form tubular nanostructures. The walls of the resulting nanotubes are maintained in position by the cooperative action of at least eight primary hydrogen bonding contacts per macrocycle. These noncovalent interactions maintain the mean planes of independent macrocycles in an approximately parallel arrangement with a plane-to-plane separation of ≈ 0.5 nm.

2.1.4 From Structural Control to Designed Properties and Functions

The examples in Figs. 2.3 and 2.4 demonstrate that modular building blocks can be assembled into target compounds with precise structural control at the picometer level through programmed sequences of synthetic steps. Indeed, modern chemical synthesis offers access to complex molecules with nanoscaled dimensions and, thus, provides cost-effective strategies for the pro-

duction and characterization of billions of engineered nanostructures in parallel. Furthermore, the high degree of structural control is accompanied by the possibility of designing specific properties into the target nanostructures. Electroactive and photoactive components can be integrated chemically into functional molecular machines [2.9]. Extensive electrochemical investigations have demonstrated that inorganic and organic compounds can exchange electrons with macroscopic electrodes [2.10]. These studies have unraveled the processes responsible for the oxidation and reduction of numerous functional groups and indicated viable design criteria to adjust the ability of molecules to accept or donate electrons [2.11]. Similarly, detailed photochemical and photophysical investigations have elucidated the mechanisms responsible for the absorption and emission of photons at the molecular level [2.12]. The vast knowledge established on the interactions between light and molecules offers the opportunity to engineer chromophoric and fluorophoric functional groups with defined absorption and emission properties [2.11, 13].

The power of chemical synthesis to deliver functional molecules is, perhaps, better illustrated by the molecular motor shown in Fig. 2.5. The preparation of this [2]rotaxane requires 12 synthetic steps starting from known precursors [2.14]. This complex molecule incorporates a Ru(II)-trisbipyridine stopper bridged to a linear tetracationic fragment by a rigid triaryl spacer. The other end of the tetracationic portion is terminated by a bulky tetraarylmethane stopper. The bipyridinium unit of this dumbbell-shaped compound is encircled by a macrocyclic polyether. No covalent bonds join the macrocyclic and linear components. Rather, hydrogen bonding and $[\pi \cdots \pi]$ stacking interactions maintain the

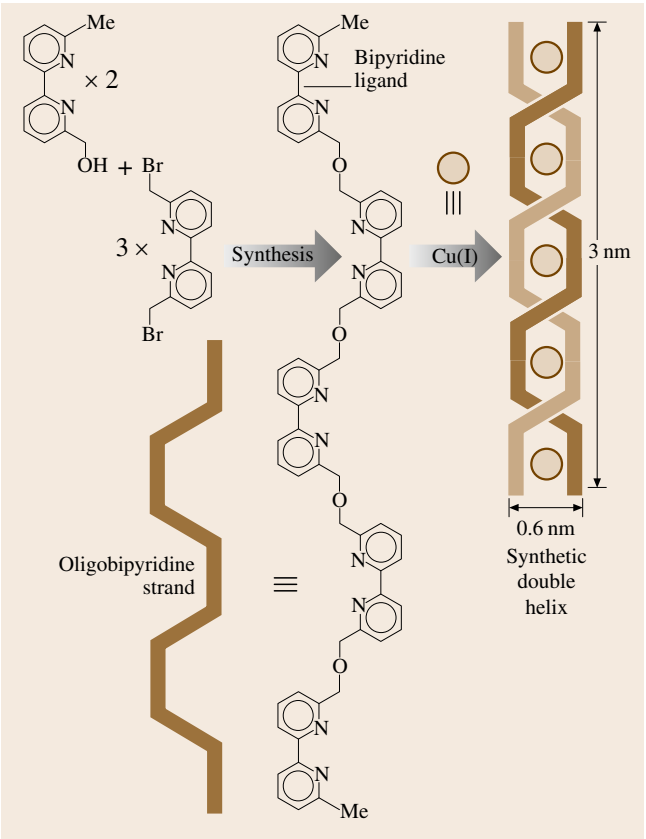

Fig. 2.3 An oligobipyridine strand can be synthesized joining five bipyridine subunits by covalent bonds. The tetrahedral coordination of pairs of bipyridine ligands by Cu(I) ions encourages the assembly two oligobipyridine strands into a double helical arrangement

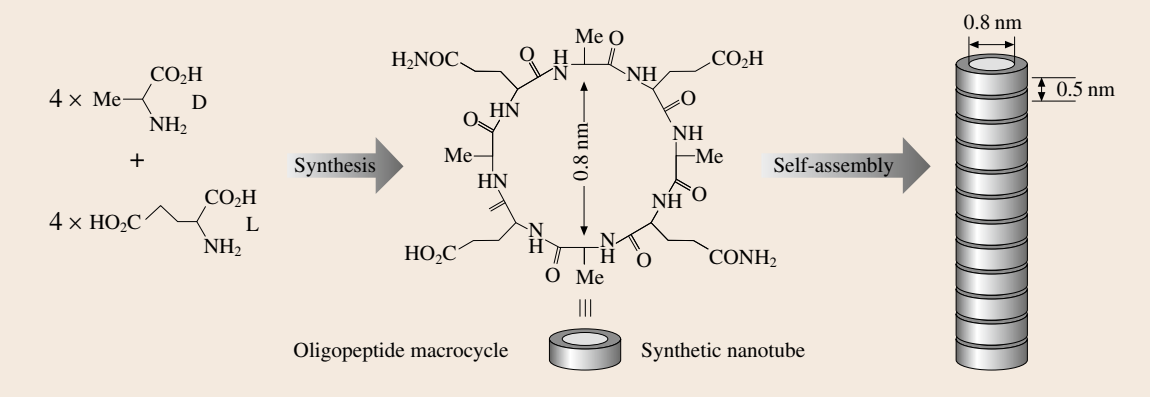

Fig. 2.4 Cyclic oligopeptides can be synthesized joining eight amino acid residues by covalent bonds. The resulting macrocycles self-assemble into nanoscaled tubelike arrays

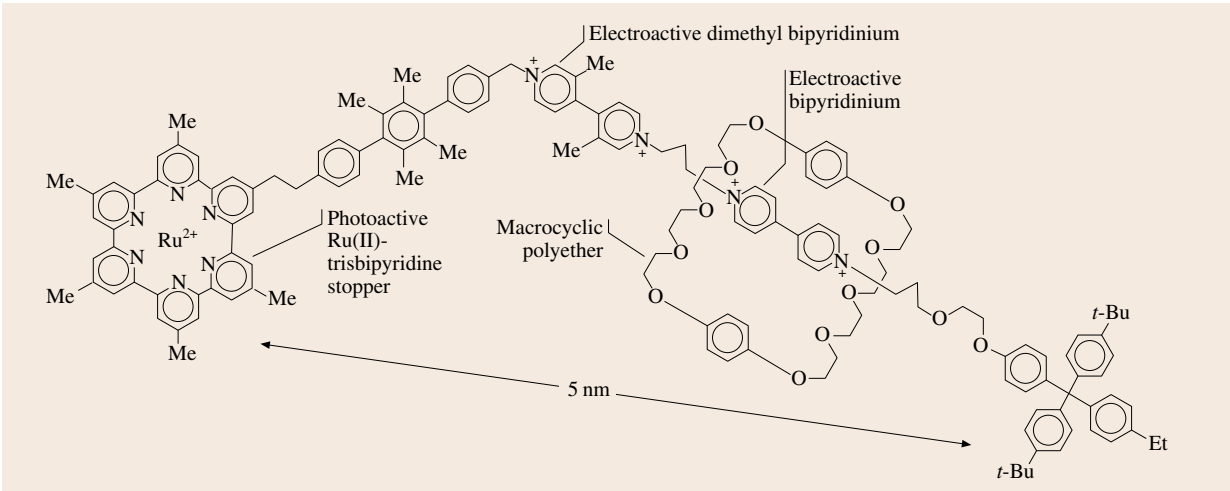

Fig. 2.5 This nanoscaled [2]rotaxane incorporates a photoactive Ru(II)-trisbipyridine stopper and two electroactive bipyridinium units. Photoinduced electron transfer from the photoactive stopper to the encircled electroactive unit forces the macrocyclic polyether to shuttle to the adjacent bipyridinium dication

macrocyclic polyether around the bipyridinium unit. In addition, mechanical constrains associated with the bulk of the two terminal stoppers prevent the macrocycle to slip off the thread. The approximate end-to-end distance for this [2]rotaxane is ≈ 5 nm.

The bipyridinium and the 3,3′-dimethyl bipyridinium units within the dumbbell-shaped component undergo two consecutive and reversible monoelectronic reductions [2.14]. The two methyl substituents on the 3,3′-dimethyl bipyridinium dication make this electroactive unit more difficult to reduce. In acetonitrile, its redox potential is ≈ 0.29 V more negative than that of the unsubstituted bipyridinium dication. Under irradiation at 436 nm in degassed acetonitrile, the excitation of the Ru(II)-trisbipyridine stopper is followed by electron transfer to the unsubstituted bipyridinium unit. In the presence of a sacrificial electron donor (triethanolamine) in solution, the photogenerated hole in the photoactive stopper is filled, and undesired back electron transfer is suppressed. The permanent and light-induced reduction of the dicationic bipyridinium unit to a radical cation depresses significantly the magnitude of the noncovalent interactions holding the macrocyclic polyether in position. As a result, the macrocycle shuttles from the reduced unit to the adjacent dicationic 3,3′-dimethyl bipyridinum. After the diffusion of molecular oxygen into the acetonitrile solution, oxidation occurs restoring the dicationic form of the bipyridinium unit and its ability to sustain strong noncovalent bonds. As a result, the macrocyclic polyether shuttles back to its original position. This amazing example of a molecular shuttle reveals that dynamic processes can be controlled reversibly at the molecular level relying on the clever integration of electroactive and photoactive fragments into functional and nanoscaled molecules.

2.2 Molecular Switches and Logic Gates

Everyday, we routinely perform dozens of switching operations. We turn on and off our personal computers, cellular phones, CD players, radios, or simple light bulbs at a click of a button. Every single time, our finger exerts a mechanical stimulation on a control device, namely a switch. The external stimulus changes the physical state of the switch closing or opening an electric circuit and enabling or preventing the passage of electrons. Overall, the switch transduces a mechanical input into an electrical output.

2.2.1 From Macroscopic to Molecular Switches

The use of switching devices is certainly not limited to electric circuits. For example, a switch at the junction

of a railroad can divert trains from one track to another. Similarly, a faucet in a lavatory pipe can block or release the flow of water. Of course, the nature of the control stimulations and the character of the final outcome vary significantly from case to case, but the operating principle behind each switching device is the same. In all cases, input stimulations reach the switch changing its physical state and producing a specific output.

The development of nanoscaled counterparts to conventional switches is expected to have fundamental scientific and technological implications. For instance, one can envisage practical applications for ultraminiaturized switches in areas ranging from biomedical research to information technology. The major challenge in the quest for nanoswitches, however, is the identification of reliable design criteria and operating principles for these innovative and fascinating devices. Chemical approaches to implement molecule-sized switches appear to be extremely promising. The intrinsically small dimensions of organic molecules coupled with the power of chemical synthesis are the main driving forces behind these exploratory investigations.

Certain organic molecules adjust their structural and electronic properties when stimulated with chemical, electrical, or optical inputs. Generally, the change is accompanied by an electrochemical or spectroscopic response. Overall, these nanostructures transduce input stimulations into detectable outputs and, appropriately, are called molecular switches [2.15, 16]. The chemical transformations associated with these switching processes are often reversible. The chemical system returns to the original state when the input signal is turned off. The interconverting states of a molecular switch can be isomers, an acid and its conjugated base, the oxidized and reduced forms of a redox active molecule, or even the complexed and uncomplexed forms of a receptor [2.9, 13, 15, 16]. The output of a molecular switch can be a chemical, electrical, and/or optical signal that varies in intensity with the interconversion process. For example, changes in absorbance, fluorescence, pH, or redox potential can accompany the reversible transformation of a molecular switch.

2.2.2 Digital Processing and Molecular Logic Gates

In present computer networks, data are elaborated electronically by microprocessor systems [2.17] and are exchanged optically between remote locations [2.18]. Data processing and communication require the encoding of information in electrical and optical signals in the form of binary digits. Using arbitrary assumptions, logic thresholds can be established for each signal and, then, 0 and 1 digits can be encoded following simple conventions. Sequences of electronic devices manipulate the encoded bits executing logic functions as a result of basic switching operations.

The three basic AND, NOT, and OR operators combine binary inputs into binary outputs following precise logic protocols [2.17]. The NOT operator converts an input signal into an output signal. When the input is 0, the output is 1. When the input is 1, the output is 0. Because of the inverse relationship between the input and output values, the NOT gate is often called *inverter* [2.19]. The OR operator combines two input signals into a single output signal. When one or both inputs are 1, the output is 1. When both inputs are 0, the output is 0. The AND gate also combines two input signals into one output signal. In this instance, however, the output is 1 only when both inputs are 1. When at least one input is 0, the output is 0.

The output of one gate can be connected to one of the inputs of another operator. A NAND gate, for example, is assembled connecting the output of an AND operator to the input of a NOT gate. Now the two input signals are converted into the final output after two consecutive logic operations. In a similar fashion, a NOR gate can be assembled connecting the output of an OR operator to the input of a NOT gate. Once again, two consecutive logic operations determine the relation between two input signals and a single output. The NAND and NOR operations are termed universal functions because any conceivable logic operation can be implemented relying only on one of these two gates [2.17]. In fact, digital circuits are fabricated routinely interconnecting exclusively NAND or exclusively NOR operators [2.19].

The logic gates of conventional microprocessors are assembled interconnecting transistors, and their input and output signals are electrical [2.19]. But the concepts of binary logic can be extended to chemical, mechanical, optical, pneumatic, or any other type of signal. First it is necessary to design devices that can respond to these stimulations in the same way transistors respond to electrical signals. Molecular switches respond to a variety of input stimulations producing specific outputs and can, therefore, be exploited to implement logic functions [2.13, 20, 21].

2.2.3 Molecular AND, NOT, and OR Gates

More than a decade ago, researchers proposed a potential strategy to execute logic operations at the molecular level [2.22]. Later, the analogy between molecular switches and logic gates was recognized in a seminal article [2.23], in which it was demonstrated that AND, NOT, and OR operations can be reproduced with fluorescent molecules. The pyrazole derivative **1** (Fig. 2.6) is a molecular NOT gate. It imposes an inverse relation between a chemical input (concentration of H^+) and an optical output (emission intensity). In a mixture of methanol and water, the fluorescence quantum yield of **1** is 0.13 in the presence of only 0.1 equivalents of H^+ [2.23]. The quantum yield drops to 0.003 when the equivalents of H^+ are 1000. Photoinduced electron transfer from the central pyrazoline unit to the pendant benzoic acid quenches the fluorescence of the protonated form. Thus, a change in H^+ concentration (I) from a low to a high value switches the emission intensity (O) from a high to a low value. The inverse relationship between the chemical input I and the optical output O translates into the truth table of a NOT operation if a positive logic convention (low = 0, high = 1) is applied to both signals. The emission intensity is high (O = 1) when the concentration of H^+ is low (I = 0). The emission intensity is low (O = 0) when the concentration of H^+ is high (I = 1).

The anthracene derivative **2** (Fig. 2.6) is a molecular OR gate. It transduces two chemical inputs (concentrations of Na^+ and K^+) into an optical output (emission intensity). In methanol, the fluorescence quantum yield is only 0.003 in the absence of metal cations [2.23]. Photoinduced electron transfer from the nitrogen atom of the azacrown fragment to the anthracene fluorophore quenches the emission. After the

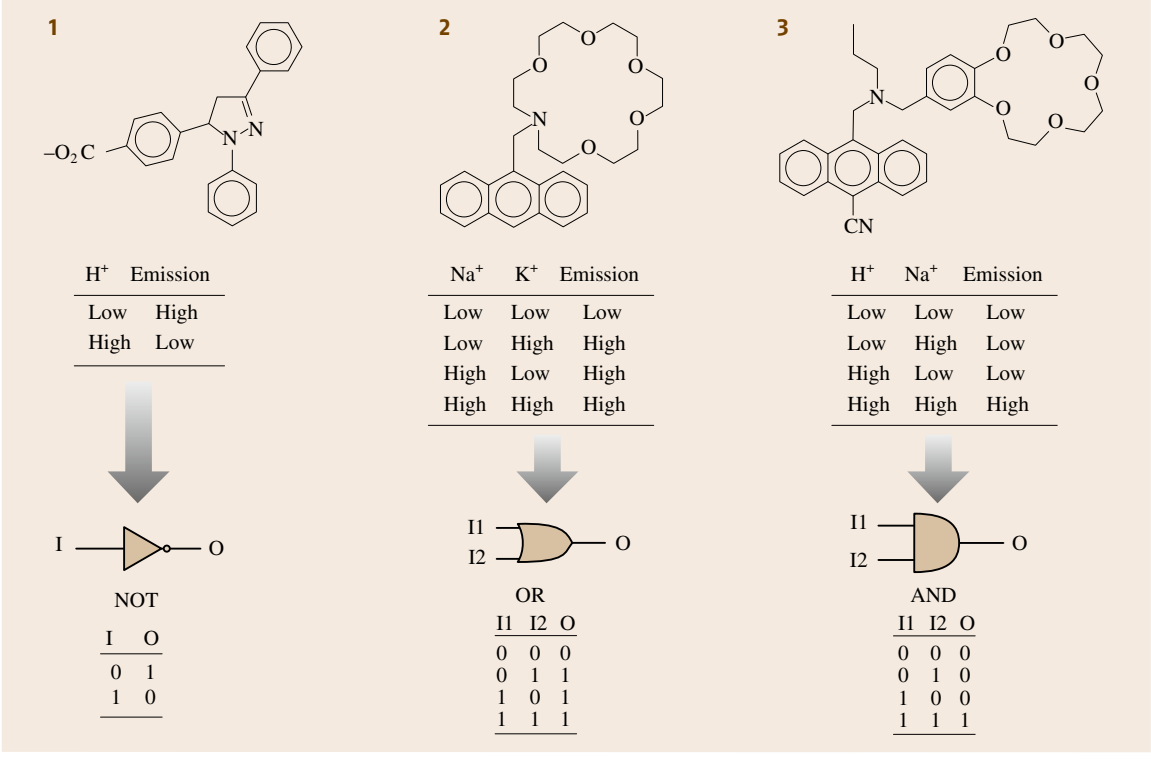

Fig. 2.6 The fluorescence intensity of the pyrazoline derivative **1** is high when the concentration of H^+ is low, and vice versa. The fluorescence intensity of the anthracene derivative **2** is high when the concentration of Na^+ and/or K^+ is high. The emission is low when both concentrations are low. The fluorescence intensity of the anthracene **3** is high only when the concentrations of H^+ and Na^+ are high. The emission is low in the other three cases. The signal transductions of the molecular switches **1**, **2**, and **3** translate into the truth tables of NOT, OR, and AND gates, respectively, if a positive logic convention is applied to all inputs and outputs (low = 0, high = 1)

addition of 1000 equivalents of either Na^+ or K^+, the quantum yield raises to 0.053 and 0.14, respectively. Similarly, the quantum yield is 0.14 when both metal cations are present in solution. The complexation of one of the two metal cations inside the azacrown receptor depresses the efficiency of the photoinduced electron transfer enhancing the fluorescence. Thus, changes in the concentrations of Na^+ (I1) and/or K^+ (I2) from low to high values switch the emission intensity (O) from a low to a high value. The relationship between the chemical inputs I1 and I2 and the optical output O translates into the truth table of an OR operation if a positive logic convention (low = 0, high = 1) is applied to all signals. The emission intensity is low (O = 0) only when the concentration of Na^+ and K^+ are low (I1 = 0, I2 = 0). The emission intensity is high (O = 1) for the other three input combinations.

The anthracene derivative **3** (Fig. 2.6) is a molecular AND gate. It transduces two chemical inputs (concentrations of H^+ and Na^+) into an optical output (emission intensity). In a mixture of methanol and *iso*-propanol, the fluorescence quantum yield is only 0.011 in the absence of H^+ or Na^+ [2.23]. Photoinduced electron transfer from either the tertiary amino group or the catechol fragment to the anthracene fluorophore quenches the emission. After the addition of either 100 equivalents of H^+ or 1000 equivalents of Na^+, a modest change of the quantum yield to 0.020 and 0.011, respectively, is observed. Instead, the quantum yield increases to 0.068 when both species are present in solution. The protonation of the amino group and the insertion of the metal cation in the benzocrown ether receptor depress the efficiency of the photoinduced electron transfer processes enhancing the fluorescence. Thus, changes in the concentrations of H^+ (I1) and Na^+ (I2) from low to high values switch the emission intensity (O) from a low to a high value. The relationship between the chemical inputs I1 and I2 and the optical output O translates into the truth table of an AND operation if a positive logic convention (low = 0, high = 1) is applied to all signals. The emission intensity is high (O = 1) only when the concentration of H^+ and Na^+ are high (I1 = 1, I2 = 1). The emission intensity is low (O = 0) for the other three input combinations.

2.2.4 Combinational Logic at the Molecular Level

The fascinating molecular AND, NOT, and OR gates illustrated in Fig. 2.6 have stimulated the design of related chemical systems able to execute the three basic logic operations and simple combinations of them [2.13, 20,21]. Most of these molecular switches convert chemical inputs into optical outputs. But the implementation of logic operations at the molecular level is not limited to the use of chemical inputs. For example, electrical signals and reversible redox processes can be exploited to modulate the output of a molecular switch [2.24]. The supramolecular assembly **4** (Fig. 2.7) executes a XNOR function relying on these operating principles. The π-electron rich tetrathiafulvalene (TTF) guest threads the cavity of a π-electron deficient bipyridinium (BIPY) host. In acetonitrile, an absorption band associated with the charge-transfer interactions between the complementary π-surfaces is observed at 830 nm. Electrical stimulations alter the redox state of either the TTF or the BIPY units encouraging the separation of the two components of the complex and the disappearance of the charge-transfer band. Electrolysis at a potential of +0.5 V oxidizes the neutral TTF unit to a monocationic state. The now cationic guest is expelled from the cavity of the tetracationic host as a result of electrostatic repulsion. Consistently, the absorption band at 830 nm disappears. The charge-transfer band, however, is restored after the exhaustive back reduction of the TTF unit at a potential of 0 V. Similar changes in the absorption properties can be induced addressing the BIPY units. Electrolysis at −0.3 V reduces the dicationic BIPY units to their monocationic forms encouraging the separation of the two components of the complex and the disappearance of the absorption band. The original absorption spectrum is restored after the exhaustive back oxidation of the BIPY units at a potential of 0 V. Thus, this supramolecular system responds to electrical stimulations producing an optical output. One of the electrical inputs (I1) controls the redox state of the TTF unit switching between 0 and +0.5 V. The other (I2) determines the redox state of the bipyridinium units switching between −0.3 and 0 V. The optical output (O) is the absorbance of the charge-transfer band. A positive logic convention (low = 0, high = 1) can be applied to the input I1 and output O. A negative logic convention (low = 1, high = 0) can be applied to the input I2. The resulting truth table corresponds to that of a XNOR circuit (Fig. 2.7). The charge-transfer absorbance is high (O = 1) only when one voltage input is low and the other is high (I1 = 0, I2 = 0) or vice versa (I1 = 1, I2 = 1). It is important to note that the input string with both I1 and I2 equal to 1 implies that input potentials of +0.5 and −0.3 V are applied simultaneously to a solution containing the supramolecular assembly **4** and not to an individual complex. Of course,

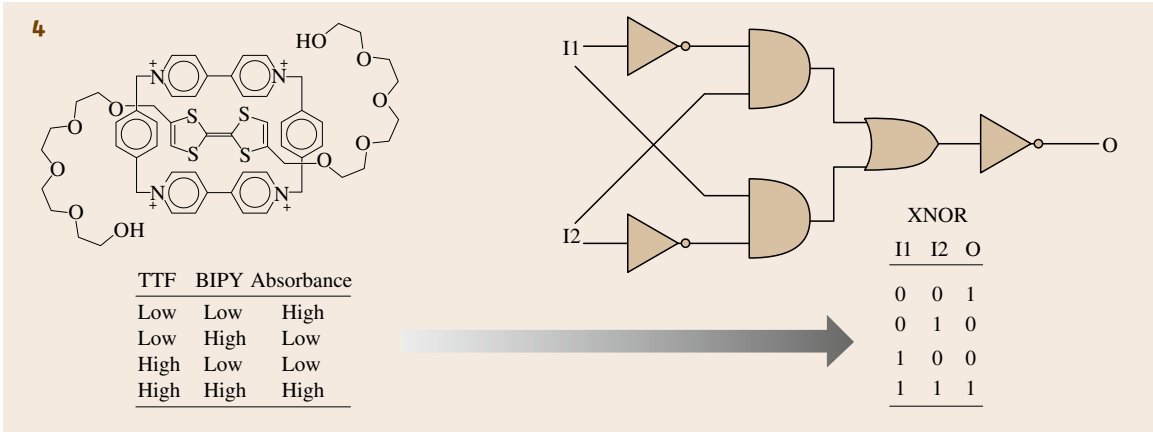

Fig. 2.7 The charge-transfer absorbance of the complex **4** is high when the voltage input addressing the tetrathiafulvalene (TTF) unit is low and that stimulating the bipyridinium (BIPY) units is high and vice versa. If a positive logic convention is applied to the TTF input and to the absorbance output (low = 0, high = 1) while a negative logic convention is applied to the BIPY input (low = 0, high = 1), the signal transduction of **4** translates into the truth table of a XNOR circuit

the concomitant oxidation of the TTF guest and reduction of the BIPY units in the very same complex would be unrealistic. In bulk solution, instead, some complexes are oxidized while others are reduced, leaving the average solution composition unaffected. Thus, the XNOR operation executed by this supramolecular system is a consequence of bulk properties and not a result of unimolecular signal transduction.

Optical inputs can be employed to operate the three-state molecular switch of Fig. 2.8 in acetonitrile solution [2.25]. This chemical system responds to three inputs producing two outputs. The three input stimulations are ultraviolet light (I1), visible light (I2), and the concentration of H^+ (I3). One of the two optical outputs is the absorbance at 401 nm (O1), which is high when the molecular switch is in the yellow-green state **6** and low in the other two cases. The other optical output is the absorbance at 563 nm (O2), which is high when the molecular switch is in the purple state **7** and low in the other two cases. The colorless spiropyran state **5** switches to the merocyanine form **7** upon irradiation with ultraviolet light. It switches to the protonated merocyanine from **6** when treated with H^+. The colored state **7** isomerizes back to **5** in the dark or upon irradiation with visible light. Alternatively, **7** switches to **6** when treated with H^+. The colored state **6** switches to **5**, when irradiated with visible light, and to **7**, after the removal of H^+. In summary, this three-state molecular switch responds to two optical inputs (I1 and I2) and one chemical input (I3) producing two optical outputs (O1 and O2). Binary digits can be encoded on each signal applying positive logic conventions (low = 0, high = 1). It follows that the three-state molecular switch converts input strings of three binary digits into output strings of two binary digits. The corresponding truth table (Fig. 2.8) reveals that the optical output O1 is high (O1 = 1) when only the input I3 is applied (I1 = 0, I2 = 0, I3 = 1), when only the input I2 is not applied (I1 = 1, I2 = 0, I3 = 0), or when all three inputs are applied (I1 = 1, I2 = 0, I3 = 0). The optical output O2 is high (O2 = 1) when only the input I1 is applied (I1 = 1, I2 = 0, I3 = 0) or when only the input I3 is not applied (I1 = 1, I2 = 0, I3 = 0). The combinational logic circuit (Fig. 2.8) equivalent to this truth table shows that all three inputs determine the output O1, while only I1 and I3 control the value of O2.

2.2.5 Intermolecular Communication

The combinational logic circuits in Figs. 2.7 and 2.8 are arrays of interconnected AND, NOT, and OR operators. The digital communication between these basic logic elements ensures the execution of a sequence of simple logic operations that results in the complex logic function processed by the entire circuit. It follows that the logic function of a given circuit can be adjusted altering the number and type of basic gates and their interconnection protocol [2.17]. This modular approach to combinational logic circuits is extremely powerful. Any logic function can be implemented connecting the appropriate combination of simple AND, NOT, and OR gates.

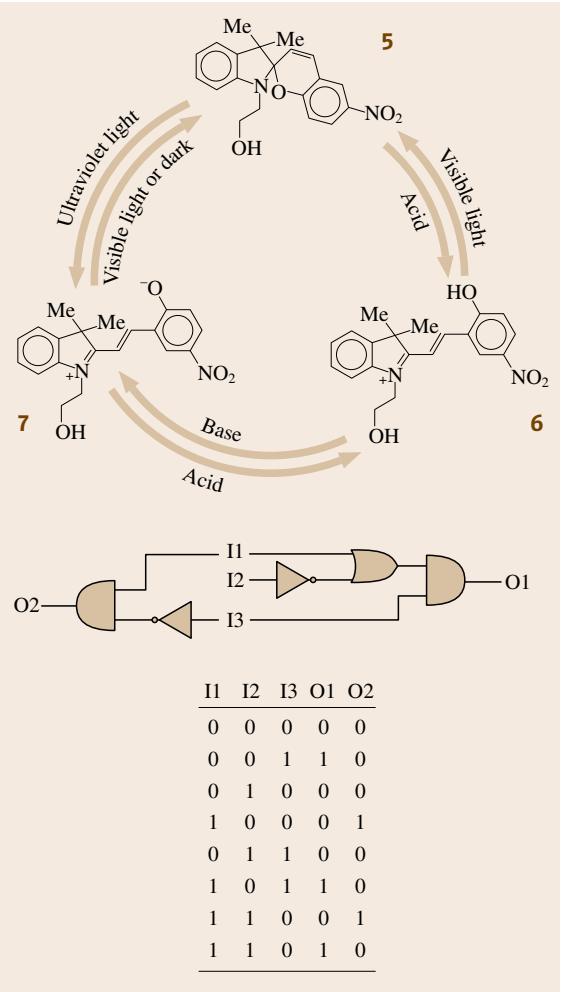

I1	I2	I3	O1	O2
0	0	0	0	0
0	0	1	1	0
0	1	0	0	0
1	0	0	0	1
0	1	1	0	0
1	0	1	1	0
1	1	0	0	1
1	1	0	1	0

Fig. 2.8 Ultraviolet light (I1), visible light (I2), and H^+ (I3) inputs induce the interconversion between the three states **5**, **6**, and **7**. The colorless state **5** does not absorb in the visible region. The yellow-green state **6** absorbs at 401 nm (O1). The purple state **7** absorbs at 563 nm (O2). The truth table illustrates the conversion of input strings of three binary digits (I1, I2, and I3) into output strings of two binary digits (O1 and O2) operated by this three-state molecular switch. A combinational logic circuit incorporating nine AND, NOT, and OR operators correspond to this particular truth table

The strategies followed so far to implement complex logic functions with molecular switches are based on the careful design of the chemical system and on the judicious choice of the inputs and outputs [2.13, 20, 21]. A specific sequence of AND, NOT, and OR operations is programmed in a single molecular switch. No digital communication between distinct gates is needed since they are built in the same molecular entity. Though extremely elegant, this strategy does not have the same versatility of a modular approach. A different molecule has to be designed, synthesized, and analyzed every single time a different logic function has to be realized. In addition, the degree of complexity that can be achieved with only one molecular switch is fairly limited. The connection of the input and output terminals of independent molecular AND, NOT, and OR operators, instead, would offer the possibility of assembling any combinational logic circuit from three basic building blocks.

In digital electronics, the communication between two logic gates can be realized connecting their terminals with a wire [2.19]. Methods to transmit binary data between distinct molecular switches are not so obvious and must be identified. Recently we developed two strategies to communicate signals between compatible molecular components. In one instance, a chemical signal is communicated between two distinct molecular switches [2.26]. They are the three-state switch illustrated in Fig. 2.8 and the two-state switch of Fig. 2.9. The merocyanine form **7** is a photogenerated base. Its *p*-nitrophenolate fragment, produced upon irradiation of the colorless state **5** with ultraviolet light, can abstract a proton from an acid present in the same solution. The resulting protonated form **6** is a photoacid. It releases a proton upon irradiation with visible light and can protonate a base co-dissolved in the same medium. The orange azopyridine **8** switches to the red-purple azopyridinium **9** upon protonation. This process is reversible, and the addition of a base restores the orange state **8**. It follows that photoinduced proton transfer can be exploited to communicate a chemical signal from **6** to **8** and from **9** to **7**. The two colored states **8** and **9** have different absorption properties in the visible region. In acetonitrile, the orange state **8** absorbs at 422 nm, and the red-purple state **9** absorbs at 556 nm. The changes in absorbance of these two bands can be exploited to monitor the photoinduced exchange of protons between the two communicating molecular switches.

The three-state molecular switch and the two-state molecular switch can be operated sequentially when dissolved in the same acetonitrile solution. In the presence of one equivalent of H^+, the two-state molecular switch is in state **9** and the absorbance at 556 nm is high (O = 1). Upon irradiation with ultraviolet light (I1 = 0), **5** switches to **7**. The photogenerated base deprotonates **9** producing **8** and **6**. As a result, the absorbance at 556 nm decreases (O = 0). Upon irradiation

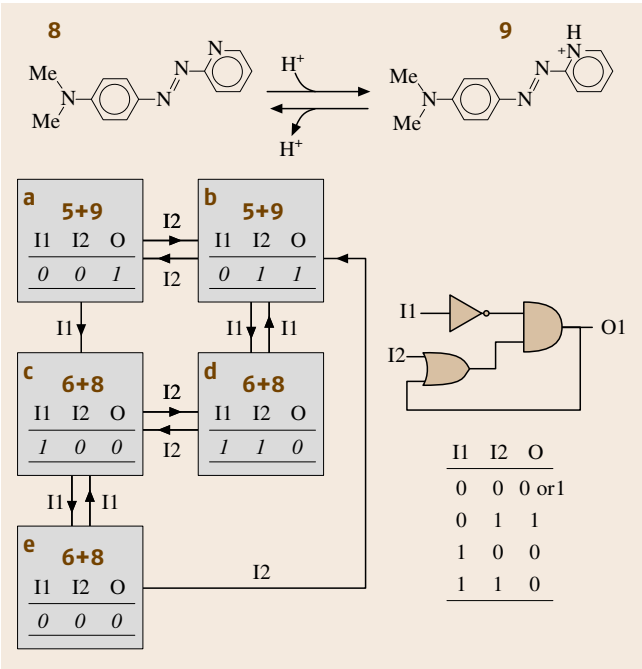

Fig. 2.9 The concentration of H^+ controls the reversible interconversion between the two states **8** and **9**. In response to ultraviolet (I1) and visible (I2) inputs, the three-state molecular switch in Fig. 2.7 modulates the ratio between these two forms and the absorbance (O) of **9** through photoinduced proton transfer. The truth table and sequential logic circuit illustrate the signal transduction behavior of the two communicating molecular switches. The interconversion between the five three-digit strings of input (I1 and I2) and output (O) data is achieved varying the input values in steps ◄

with visible light (I2 = 1), **6** switches to **5** releasing H^+. The result is the protonation of **8** to form **9** and restore the high absorbance at 556 nm (O = 1). In summary, the three-state molecular switch transduces two optical inputs (I1 = ultraviolet light, I2 = visible light) into a chemical signal (proton transfer) that is communicated to the two-state molecular switch and converted into a final optical output (O = absorbance at 556 nm).

The logic behavior of the two communicating molecular switches is significantly different from those of the chemical systems illustrated in Figs. 2.6–2.8 [2.26]. The truth table in Fig. 2.9 lists the four possible combinations of two-digit input strings and the corresponding one-digit output. The output digit O for the input strings 01, 10, and 11 can take only one value. In fact, the input string 01 is transduced into a 1, and the input strings 10 and 11 are converted into 0. Instead, the output digit O for the input string 00 can be either 0 or 1. The sequence of events leading to the input string 00 determines the value of the output. The boxes **a**–**e** in Fig. 2.9 illustrates this effect. They correspond to the five three-digit input/output strings. The transformation of one box into any of the other four is achieved in one or two steps by changing the values of I1 and/or I2. In two instances (**a** and **b**), the two-state molecular switch is in state **9**, and the output signal is high (O = 1). In the other three cases (**c**, **d**, and **e**), the two-state molecular switch is in state **8**, and the output signal is low (O = 0). The strings 000 (**e**) and 001 (**a**) correspond to the first entry of the truth table. They share the same input digits but differ in the output value. The string 000 (**e**) can be obtained only from the string 100 (**c**) varying the value of I1. Similarly, the string 001 (**a**) can be accessed only from the string 011 (**b**) varying the value of I2. In both transformations, the output digit remains unchanged. Thus, the value of O1 in the parent string is memorized and maintained in the daughter string when both inputs become 0. This memory effect is the fundamental operating principle of sequential logic circuits [2.17], which are used extensively to assemble the memory elements of modern microprocessors. The sequential logic circuit equivalent to the truth table of the two communicating molecular switches is also shown in Fig. 2.9. In this circuit, the input data I1 and I2 are combined through NOT, OR, and AND operators. The output of the AND gate O is also an input of the OR gate and controls, together with I1 and I2, the signal transduction behavior.

The other strategy for digital transmission between molecules is based on the communication of optical signals between the three-state molecular switch (Fig. 2.8) and fluorescent compounds [2.27]. In the optical network of Fig. 2.10, three optical signals travel from an excitation source to a detector after passing through two quartz cells. The first cell contains an equimolar acetonitrile solution of naphthalene, anthracene, and tetracene. The second cell contains an acetonitrile solution of the three-state molecular switch. The excitation source sends three consecutive monochromatic light beams to the first cell stimulating the emission of the three fluorophores. The light emitted in the direction perpendicular to the exciting beam reaches the second cell. When the molecular switch is in state **5**, the naphthalene emission at 335 nm is absorbed and a low intensity output (O1) reaches the detector. Instead, the anthracene and tetracene emissions at 401 and 544 nm,

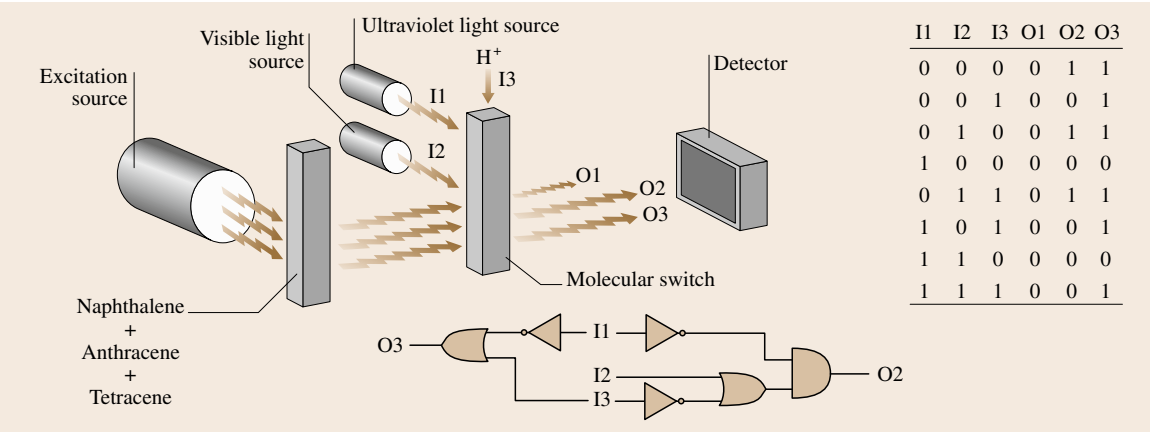

I1	I2	I3	O1	O2	O3
0	0	0	0	1	1
0	0	1	0	0	1
0	1	0	0	1	1
1	0	0	0	0	0
0	1	1	0	1	1
1	0	1	0	0	1
1	1	0	0	0	0
1	1	1	0	0	1

Fig. 2.10 The excitation source sends three monochromatic light beams (275, 357, and 441 nm) to a quartz cell containing an equimolar acetonitrile solution of naphthalene, anthracene and tetracene. The three fluorophores absorb the exciting beams and reemit at 305, 401, and 544 nm, respectively. The light emitted in the direction perpendicular to the exciting beams passes through another quartz cell containing an acetonitrile solution of the three-state molecular switch shown in Fig. 2.7. Ultraviolet (I1), visible (I2), and H^+ (I3) inputs control the interconversion between the three states of the molecular switch. They determine the intensity of the optical outputs reaching the detector and correspond to the naphthalene (O1), anthracene (O2), and tetracene (O3) emissions. The truth table and equivalent combinational logic illustrate the relation between the three inputs and the three outputs. The output O1 is always 0, and it is not influenced by the three inputs. Only two inputs determine the value of O3, while all of them control the output O2

respectively, pass unaffected and high intensity outputs (O2 and O3) reach the detector. When the molecular switch is in state **6**, the naphthalene and anthracene emissions are absorbed and only the tetracene emission reaches the detector (O1 = 0, O2 = 0, O3 = 1). When the molecular switch is state **7**, the emission of all three fluorophores is absorbed (O1 = 0, O2 = 0, O3 = 0). The interconversion of the molecular switch between the three states is induced addressing the second cell with ultraviolet (I1), visible (I2) and H^+ (I3) inputs. Thus, three independent optical outputs (O1, O2 and O3) can be modulated stimulating the molecular switch with two optical and one chemical input. The truth table in Fig. 2.10 illustrates the relation between the three inputs (I1, I2 and I3) and the three outputs (O1, O2 and O3), when positive logic conventions are applied to all signals. The equivalent logic circuit shows that all three inputs control the anthracene channel O2, but only I1 and I3 influence the tetracene channel O3. Instead, the intensity of the naphthalene channel O1 is always low, and it is not affected by the three inputs.

The operating principles of the optical network in Fig. 2.10 can be simplified to implement all-optical logic gates. The chemical input inducing the formation of the protonated form **6** of the molecular switch can be eliminated. The interconversion between the remaining two states **5** and **7** can be controlled relying exclusively on ultraviolet inputs. Indeed, ultraviolet irradiation induces the isomerization of the colorless form **5** to the colored species **7**, which reisomerizes to the original state in the dark. Thus, a single ultraviolet source is sufficient to control the switching from **5** to **7** and vice versa. On the basis of these considerations, all-optical NAND, NOR, and NOT gates can be implemented operating sequentially or in parallel from one to three independent switching elements [2.28]. For example, the all-optical network illustrated in Fig. 2.11 is a three-input NOR gate. A monochromatic optical signal travels from a visible source to a detector. Three switching elements are aligned along the path of the traveling light. They are quartz cells containing an acetonitrile solution of the molecular switch shown in Fig. 2.8. The interconversion of the colorless form **5** into the purple isomer **7** is induced stimulating the cell with an ultraviolet input. The reisomerization from **7** to **5** occurs spontaneously, as the ultraviolet sources is turned off. Using three distinct ultraviolet sources, the three switching elements can be controlled independently.

The colorless form **5** does not absorb in the visible region, while the purple isomer **7** has a strong absorption band at 563 nm. Thus, a 563 nm optical signal leaving the visible source can reach the detector

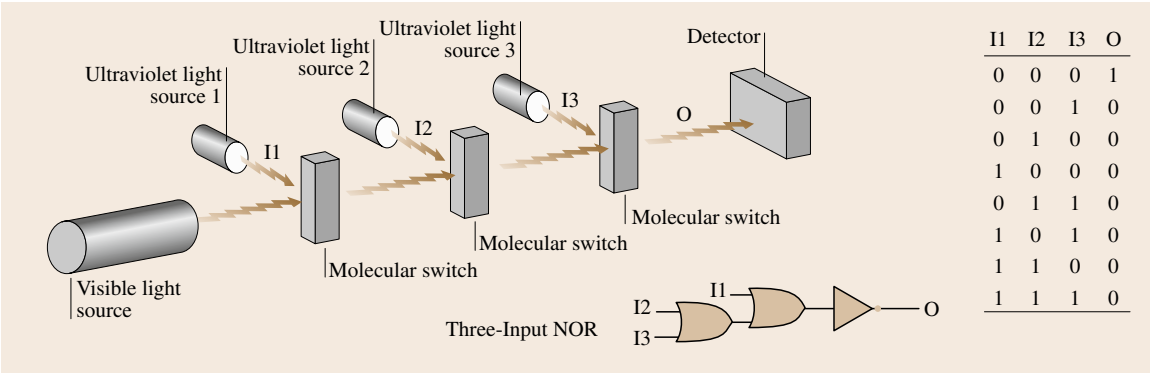

I1	I2	I3	O
0	0	0	1
0	0	1	0
0	1	0	0
1	0	0	0
0	1	1	0
1	0	1	0
1	1	0	0
1	1	1	0

Fig. 2.11 The visible source sends a monochromatic beam (563 nm) to the detector. The traveling light is forced to pass through three quartz cells containing the molecular switch illustrated in Fig. 2.7. The three switching elements are operated by independent ultraviolet inputs. When at least one of them is on, the associated molecular switch is in the purple form **7**, which can absorb and block the traveling light. The truth table and equivalent logic circuit illustrate the relation between the three inputs I1, I2, and I3 and the optical output O

unaffected only if all three switching elements are in the nonabsorbing state **5**. If one of the three ultraviolet inputs I1, I2, or I3 is turned on, the intensity of the optical output O drops to 3–4% of its original value. If two or three ultraviolet inputs are turned on simultaneously, the optical output drops to 0%. Indeed, the photogenerated state **7** absorbs and blocks the traveling light. Applying positive logic conventions to all signals, binary digits can be encoded in the three optical inputs and in the optical output. The resulting truth table is illustrated in Fig. 2.11. The output O is 1 only if all three inputs I1, I2, or I3 are 0. The output O is 0 if at least one of the three inputs I1, I2, or I3 is 1. This signal transduction corresponds to that executed by a three-input NOR gate, which is a combination of one NOT and two OR operators.

2.3 Solid State Devices

The fascinating chemical systems illustrated in Figs. 2.6–2.11 demonstrate that logic functions can be implemented relying on the interplay between designed molecules and chemical, electrical and/or optical signals [2.13, 20, 21].

2.3.1 From Functional Solutions to Electroactive and Photoactive Solids

These molecular switches, however, are operated exclusively in solution and remain far from potential applications in information technology at this stage. The integration of liquid components and volatile organic solvents in practical digital devices is hard to envisage. Furthermore, the logic operations executed by these chemical systems rely on bulk addressing. Although the individual molecular components have nanoscaled dimensions, macroscopic collections of them are employed for digital processing. In some instances, the operating principles cannot even be scaled down to the unimolecular level. Often bulk properties are responsible for signal transduction. For example, a single fluorescent compound **2** cannot execute an OR operation. Its azacrown appendage can accommodate only one metal cation. As a result, an individual molecular switch can respond to only one of the two chemical inputs. It is a collection of numerous molecular switches dissolved in an organic solvent that responds to both inputs enabling an OR operation.

The development of miniaturized molecule-based devices requires the identification of methods to transfer the switching mechanisms developed in solution to the solid state [2.29]. Borrowing designs and fabrication strategies from conventional electronics, researchers are starting to explore the integration of molecular components into functional circuits and devices [2.30–33]. Generally, these strategies combine lithography and surface chemistry to assemble nanometer-thick organic films on the surfaces of microscaled or nanoscaled

electrodes. Two main approaches for the deposition of organized molecular arrays on inorganic supports have emerged so far. In one instance, amphiphilic molecular building blocks are compressed into organized monolayers at air/water interfaces. The resulting films can be transferred on supporting solids employing the Langmuir–Blodgett technique [2.34]. Alternatively, certain molecules can be designed to adsorb spontaneously on the surfaces of compatible solids from liquid or vapor phases. The result is the self-assembly of organic layers on inorganic supports [2.35].

2.3.2 Langmuir–Blodgett Films

Films of amphiphilic molecules can be deposited on a variety of solid supports employing the Langmuir–Blodgett technique [2.34]. This method can be extended to electroactive compounds incorporating hydrophilic and hydrophobic groups. For example, the amphiphile **10** (Fig. 2.12) has a hydrophobic hexadecyl tail attached to a hydrophilic bipyridinium dication [2.36, 37]. This compound dissolves in mixtures of chloroform and methanol, but it is not soluble in moderately concentrated aqueous solutions of sodium perchlorate. Thus the spreading of an organic solution of **10** on an aqueous sodium perchlorate subphase affords a collection of disorganized amphiphiles floating on the water surface (Fig. 2.12), after the organic solvent has evaporated. The molecular building blocks can be compressed into a monolayer with the aid of a moving barrier. The hydrophobic tails align away from the aqueous phase. The hydrophilic dicationic heads and the accompanying perchlorate counterions pack to form an organized monolayer at the air/water interface. The compression process can be monitored recording the surface pressure (π)-area per molecule (A) isotherm, which indicates a limiting molecular area of $\approx 50\,\text{Å}^2$. This value is larger than the projected area of an oligomethylene chain. It correlates reasonably, however, with the overall

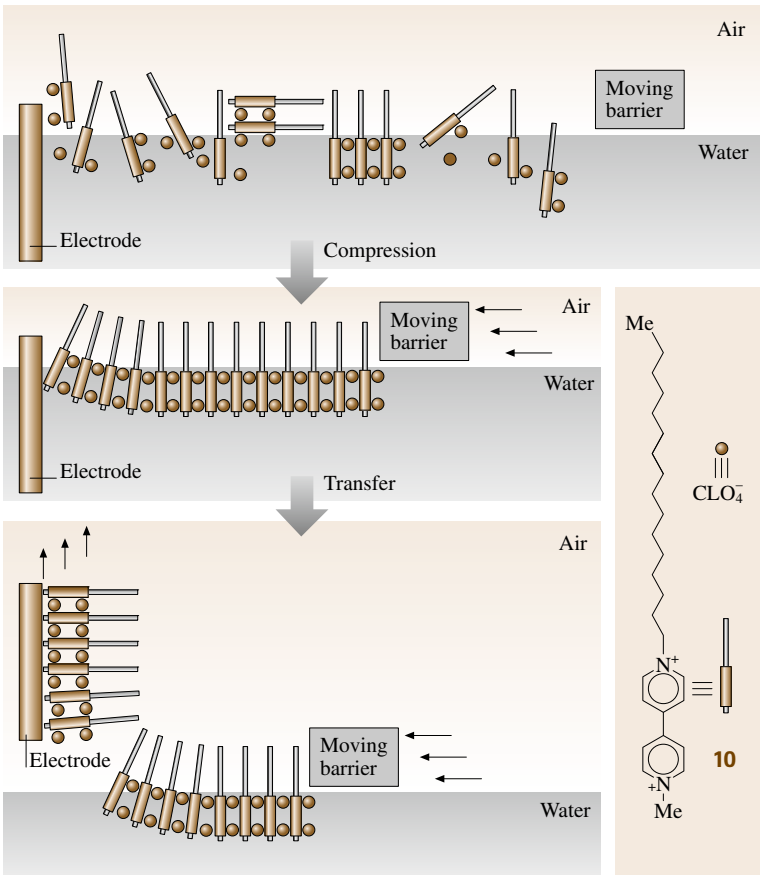

Fig. 2.12 The compression of the amphiphilic dication **10** with a moving barrier results in the formation of a packed monolayer at the air/water interface. The lifting of an electrode pre-immersed in the aqueous subphase encourages the transfer of part of the monolayer on the solid support

area of a bipyridinium dication plus two perchlorate anions.

The monolayer prepared at the air/water interface (Fig. 2.12) can be transferred on the surface of a indium-tin oxide electrode pre-immersed in the aqueous phase. The slow lifting of the solid support drags the monolayer away from the aqueous subphase. The final result is the coating of the electrode with an organic film containing electroactive bipyridinium building blocks. The modified electrode can be integrated in a conventional electrochemical cell to probe the redox response of the electroactive layer. The resulting cyclic voltammograms reveal the characteristic waves for the first reduction process of the bipyridinium dications, confirming the successful transfer of the electroactive amphiphiles from the air/water interface to the electrode surface. The integration of the redox waves indicates a surface coverage of $\approx 4\times10^{10}$ mol cm^{-2}. This value corresponds to a molecular area of ≈ 40 Å^2 and is in excellent agreement with the limiting molecular area of the π–A isotherm.

These seminal experiments demonstrate that electroactive amphiphiles can be organized into uniform monolayers at the air/water interface and then transferred efficiently on the surface of appropriate substrates to produce electrode/monolayer junctions. The resulting electroactive materials can become the functional components of molecule-based devices. For example, bipyridinium-based photodiodes can be fabricated following this approach [2.38,39]. Their operating principles rely on photoinduced electron transfer from chromophoric units to bipyridinium acceptors. The electroactive and photoactive amphiphile **11** (Fig. 2.13) incorporates hydrophobic ferrocene and pyrene tails and a hydrophilic bipyridinium head. Chloroform solutions of **11** containing ten equivalents of arachidic acid can be spread on an aqueous calcium chloride subphase in a Langmuir trough. The amphiphiles can be compressed into a mixed monolayer, after the evaporation of the organic solvent. Pronounced steps in the corresponding π–A isotherm suggest that the bulky ferrocene and pyrene groups are squeezed away from the water surface. In the final arrangement, both photoactive groups align above the hydrophobic dication.

A mixed monolayer of **11** and arachidic acid can be transferred from the air/water interface to the surface of a transparent gold electrode following the methodology illustrated for the system in Fig. 2.12. The coated electrode can be integrated in a conventional electrochemical cell. Upon irradiation at 330 nm under an inert atmosphere, an anodic photocurrent of ≈ 2 nA develops at a potential of 0 V relative to a saturated calomel electrode. Indeed, the illumination of the electroactive monolayer induces the electron transfer from the pyrene appendage to the bipyridinium acceptor and then from the reduced acceptor to the electrode. A second intramolecular electron transfer from the ferrocene donor to the oxidized pyrene fills its photogenerated hole. Overall, a unidirectional flow of electrons across the monolayer/electrode junction is established under the influence of light.

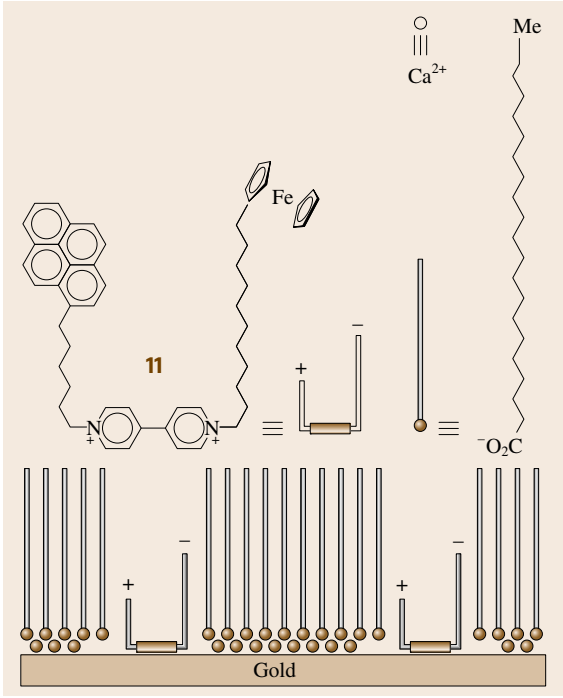

Fig. 2.13 Mixed monolayers of the amphiphile **11** and arachidic acid can be transferred from the air/water interface to the surface of an electrode to generate a molecule-based photodiode

The ability to transfer electroactive monolayers from air/water interfaces to electrode surfaces can be exploited to fabricate molecule-based electronic devices. In particular, arrays of interconnected electrode/monolayer/electrode tunneling junctions can be assembled combining the Langmuir–Blodgett technique with electron beam evaporation [2.33]. Figure 2.14 illustrates a schematic representation of the resulting devices. Initially, parallel fingers are patterned on a silicon wafer with a silicon dioxide overlayer by electron beam evaporation. The bottom electrodes deposited on the support can be either aluminum wires

covered by an aluminum oxide or *n*-doped silicon lines with silicon dioxide overlayers. Their widths are ≈ 6 or 7 μm, respectively. The patterned silicon chip is immersed in the aqueous subphase of a Langmuir trough prior to monolayer formation. After the compression of electroactive amphiphiles at the air/water interface, the substrate is pulled out of the aqueous phase to encourage the transfer of the molecular layer on the parallel bottom electrodes as well as on the gaps between them. Then, a second set of electrodes orthogonal to the first is deposited through a mask by electron beam evaporation. They consist of a titanium underlayer plus an aluminum overlayer. Their thicknesses are ≈ 0.05 and 1 μm, respectively, and their width is ≈ 10 μm. In the final assembly, portions of the molecular layer become sandwiched between the bottom and top electrodes. The active areas of these electrode/monolayer/electrode junctions are ≈ 60–70 μm^2 and correspond to ≈ 10^6 molecules.

The [2]rotaxane **12** (Fig. 2.14) incorporates a macrocyclic polyether threaded onto a bipyridinium-based backbone [2.40, 41]. The two bipyridinium dications are bridged by a *m*-phenylene spacer and terminated by tetraarylmethane appendages. These two bulky groups trap mechanically the macrocycle preventing its dissociation from the tetracationic backbone. In addition, their hydrophobicity complements the hydrophilicity of the two bipyridinium dications imposing amphiphilic character on the overall molecular assembly. This compound does not dissolve in aqueous solutions and can be compressed into organized monolayers at air/water interfaces. The corresponding π–A isotherm reveals a limiting molecular area of ≈ 130 $Å^2$. This large value is a consequence of the bulk associated with the hydrophobic tetraarylmethane tails and the macrocycle encircling the tetracationic backbone.

Monolayers of the [2]rotaxane **12** can be transferred from the air/water interface to the surfaces of the bottom aluminum/aluminum oxide electrodes of a patterned silicon chip with the hydrophobic tetraarylmethane groups pointing away from the supporting substrate. The subsequent assembly of a top titanium/aluminum electrode

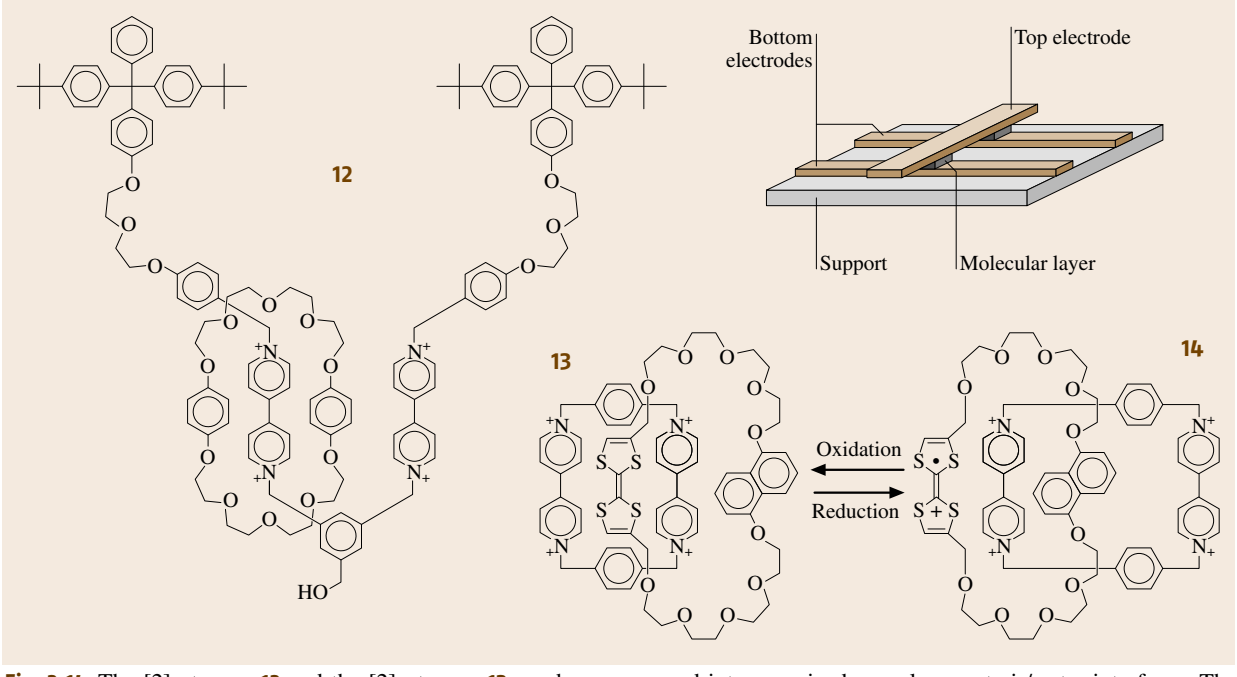

Fig. 2.14 The [2]rotaxane **12** and the [2]catenane **13** can be compressed into organized monolayers at air/water interfaces. The resulting monolayers can be transferred on the bottom electrodes of a patterned silicon support. After the deposition of a top electrode, electrode/monolayer/electrode junctions can be assembled. Note that only the portion of the monolayer sandwiched between the top and bottom electrodes is shown in the diagram. The oxidation of the tetrathiafulvalene unit of the [2]catenane **13** is followed by the circumrotation of the macrocyclic polyether to afford the [2]catenane **14**. The process is reversible, and the reduction of the cationic tetrathiafulvalene unit restores the original state

affords electrode/monolayer/electrode junctions. Their current/voltage signature can be recorded grounding the top electrode and scanning the potential of the bottom electrode. A pronounced increase in current is observed when the potential is lowered below -0.7 V. Under these conditions, the bipyridinium-centered LUMOs mediate the tunneling of electrons from the bottom to the top electrode leading to a current enhancement. A similar current profile is observed if the potential is returned to 0 and then back to -2 V. Instead, a modest increase in current in the opposite direction is observed when the potential is raised above $+0.7$ V. Presumably, this trend is a result of the participation of the phenoxy-centered HOMOs in the tunneling process. After a single positive voltage pulse, however, no current can be detected if the potential is returned to negative values. In summary, the positive potential scan suppresses irreversibly the conducting ability of the electrode/molecule/electrode junction. The behavior of this device correlates with the redox response of the [2]rotaxane **12** in solution. Cyclic voltammograms reveal reversible monoelectronic reductions of the bipyridinium dications. But they also show two irreversible oxidations associated, presumably, with the phenoxy rings of the macrocycle and tetraarylmethane groups. These observations suggest that a positive voltage pulse applied to the electrode/monolayer/electrode junction oxidizes irreversibly the sandwiched molecules suppressing their ability to mediate the transfer of electrons from the bottom to the top electrode under a negative bias.

The device incorporating the [2]rotaxane **13** can be exploited to implement simple logic operations [2.40]. The two bottom electrodes can be stimulated with voltage inputs (I1 and I2) while measuring a current output (O) at the common top electrode. When at least one of the two inputs is high (0 V), the output is low (< 0.7 nA). When both inputs are low (-2 V), the output is high (≈ 4 nA). If a negative logic convention is applied to the voltage inputs (low $= 1$, high $= 0$) and a positive logic convention is applied to the current output (low $= 0$, high $= 1$), the signal transduction behavior translates into the truth table of an AND gate. The output O is 1 only when both inputs are 1. Instead, an OR operation can be executed if the logarithm of the current is considered as the output. The logarithm of the current is -12 when both voltage inputs are 0 V. It raises to ≈ -9 when one or both voltage inputs are lowered to -2 V. This signal transduction behavior translates into the truth table of an OR gate if a negative logic convention is applied to the voltage inputs (low $= 1$, high $= 0$) and a positive logic convention is applied to the current output (low $= 0$, high $= 1$). The output O is 1 when at least one of the two inputs is 1.

The [2]catenane **13** (Fig. 2.14) incorporates a macrocyclic polyether interlocked with a tetracationic cyclophane [2.42, 43]. Organic solutions of the hexafluorophosphate salt of this [2]catenane and six equivalents of the sodium salt of dimyristoylphosphatidic acid can be co-spread on the water surface of a Langmuir trough [2.44]. The sodium hexafluorophosphate formed dissolves in the supporting aqueous phase, while the hydrophilic bipyridinium cations and the amphiphilic anions remain at the interface. Upon compression, the anions align their hydrophobic tails away from the water surface forming a compact monolayer above the cationic bipyridinium derivatives. The corresponding π–A isotherm indicates limiting molecular areas of ≈ 125 Å^2. This large value is a consequence of the bulk associated with the two interlocking macrocycles.

Monolayers of the [2]catenane **13** can be transferred from the air/water interface to the surfaces of the bottom n-doped silicon/silicon dioxide electrodes of a patterned silicon chip with the hydrophobic tails of the amphiphilic anions pointing away from the supporting substrate [2.45, 46]. The subsequent assembly of a top titanium/aluminum electrode affords electrode/monolayer/electrode arrays. Their junction resistance can be probed grounding the top electrode and maintaining the potential of the bottom electrode at $+0.1$ V. If a voltage pulse of $+2$ V is applied to the bottom electrode before the measurement, the junction resistance probed is ≈ 0.7 GΩ. After a pulse of -2 V applied to the bottom electrode, the junction resistance probed at $+0.1$ V drops ≈ 0.3 GΩ. Thus, alternating positive and negative voltage pulses can switch reversibly the junction resistance between high and low values. This intriguing behavior is a result of the redox and dynamic properties of the [2]catenane **13**.

Extensive spectroscopic and crystallographic studies [2.42, 43] demonstrated that the tetrathiafulvalene unit resides preferentially inside the cavity of the tetracationic cyclophane of the [2]catenane **13** (Fig. 2.14). Attractive [$\pi \cdots \pi$] stacking interactions between the neutral tetrathiafulvalene and the bipyridinium dications are responsible for this co-conformation. Oxidation of the tetrathiafulvalene generates a cationic form that is expelled from the cavity of the tetracationic cyclophane. After the circumrotation of the macrocyclic polyether, the oxidized tetrathiafulvalene is exchanged with the neutral 1,5-dioxynaphthalene producing the [2]catenane **14** (Fig. 2.14). The reduction of the tetrathiafulvalene back to its neutral state

is followed by the circumrotation of the macrocyclic polyether, which restores the original state **14**. The voltage pulses applied to the bottom electrode of the electrode/monolayer/junction oxidize and reduce the tetrathiafulvalene unit inducing the interconversion between the forms **13** and **14**. The difference in the stereoelectronic properties of these two states translates into distinct current/voltage signatures. Indeed, their ability to mediate the tunneling of electrons across the junction differs significantly. As a result, the junction resistance probed at a low voltage after an oxidizing pulse is significantly different from that determined under the same conditions after a reducing pulse.

2.3.3 Self-Assembled Monolayers

In the examples illustrated in Figs. 2.12–2.14, monolayers of amphiphilic and electroactive derivatives are assembled at air/water interfaces and then transferred on the surfaces of appropriate substrates. An alternative strategy to coat electrodes with molecular layers relies on the ability of certain compounds to adsorb spontaneously on solid supports from liquid or vapor phases [2.35]. In particular, the affinity of certain sulfurated functional groups for gold can be exploited to encourage the self-assembly of organic molecules on microscaled and nanoscaled electrodes.

The electrode/monolayer/electrode junction in Fig. 2.15 incorporates a molecular layer between two gold electrodes mounted on a silicon nitride support. This device can be fabricated combining chemical vapor deposition, lithography, anisotropic etching, and self-assembly [2.47]. Initially, a silicon wafer is coated with a 50 nm thick layer of silicon nitride by low pressure chemical vapor deposition. Then, a square of $400 \times 400\,\mu m^2$ is patterned on one side of the coated wafer by optical lithography and reactive ion etching. Anisotropic etching of the exposed silicon up to the other side of the wafer leaves a suspended silicon nitride membrane of $40 \times 40\,\mu m^2$. Electron beam lithography and reactive ion etching can be used to carve a bowl-shaped hole (diameter = 30–50 nm) in the membrane. Evaporation of gold on the membrane fills the pore producing a bowl-shaped electrode. Immersion of the substrate in a solution of the thiol **15** results in the self-assembly of a molecular layer on the narrow part of the bowl-shaped electrode. The subsequent evaporation of a gold film on the organic monolayer produces an electrode/monolayer/electrode junction (Fig. 2.15) with a contact area of less than $2000\,nm^2$ and ≈ 1000 molecules.

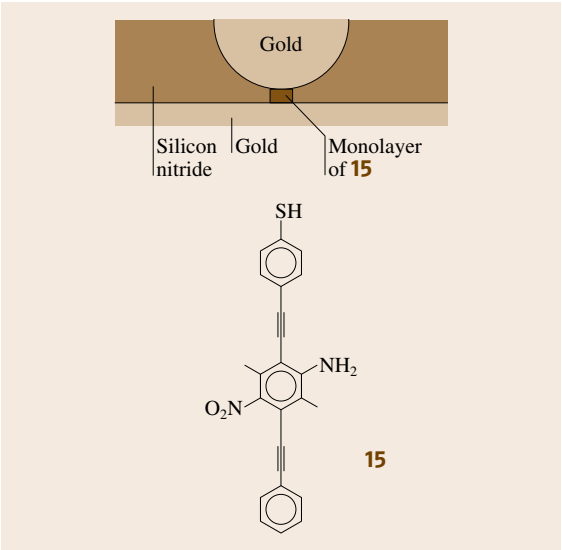

Fig. 2.15 A monolayer of the thiol **15** is embedded between two gold electrodes maintained in position by a silicon nitride support

Under the influence of voltage pulses applied to one of the two gold electrodes in Fig. 2.15, the conductivity of the sandwiched monolayer switches reversibly between low and high values [2.48]. In the initial state, the monolayer is in a low conducting mode. A current output of only 30 pA is detected, when a probing voltage of +0.25 V is applied to the bowl-shaped electrode. If the same electrode is stimulated with a short voltage pulse of +5 V, the monolayer switches to a high conducting mode. Now a current output of 150 pA is measured at the same probing voltage of +0.25 V. Repeated probing of the current output at various intervals of time indicates that the high conducting state is memorized by the molecule-based device, and it is retained for more than 15 min. The low conducting mode is restored after either a relatively long period of time or the stimulation of the bowl-shaped electrode with a reverse voltage pulse of −5 V. Thus the current output switches from a low to a high value, if a high voltage input is applied. It switches from a high to a low value, under the influence of a low voltage pulse. This behavior offers the opportunity to store and erase binary data in analogy to a conventional random access memory [2.17]. Binary digits can be encoded on the current output of the molecule-based device applying a positive logic convention (low = 0, high = 1). It follows that a binary 1 can be stored in the molecule-based device applying a high voltage

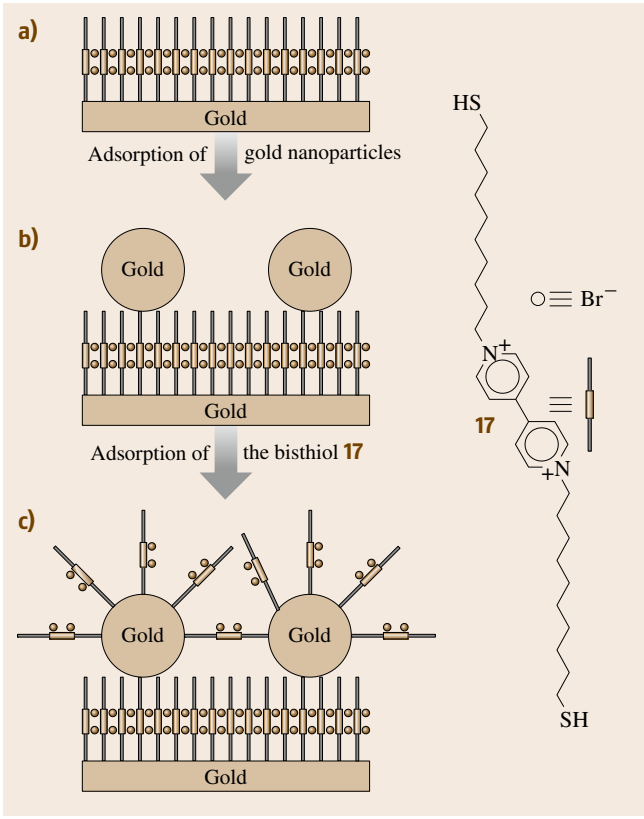

Fig. 2.16 **(a)** The bisthiol **16** self-assembles on gold electrodes as a result of thiolate–gold bond formation. **(b)** Gold nanoparticles adsorb spontaneously on the molecular layer. **(c)** Exposure of the composite assembly to a solution of **16** results in the formation of an additional molecular layer on the surface of the gold nanoparticles

input, and it can be erased applying a low voltage input [2.48].

The ability of thiols to self-assemble on the surface of gold can be exploited to fabricate nanocomposite materials integrating organic and inorganic components. For example, the bisthiol **16** forms monolayers (Fig. 2.16a) on gold electrodes with surface coverages of $\approx 4.1\times10^{10}$ mol cm^2 [2.49, 50]. The formation of a thiolate–gold bond at one of the two thiol ends of **16** is responsible for adsorption. The remaining thiol group points away from the supporting surface and can be exploited for further functionalization. Gold nanoparticles adsorb on the molecular layer (Fig. 2.16b), once again, as a result of thiolate–gold bond formation. The immersion of the resulting material in a methanol solution of **16** encourages the adsorption of an additional organic layer (Fig. 2.16c) on the composite material. Following these procedures, up to ten alternating organic and inorganic layers can be deposited on the electrode surface. The resulting assembly can mediate the unidirectional electron transfer from the supporting electrode to redox active species in solution. For example, the cyclic voltammogram of the $[Ru(NH_3)_6]^{3+/2+}$ couple recorded with a bare gold electrode reveals a reversible reduction process. In the presence of ten alternating molecular and nanoparticle layers on the electrode surface, the reduction potential shifts by ≈ -0.2 V and the back oxidation wave disappears. The pronounced potential shift indicates that $[Ru(NH_3)_6]^{3+}$ accepts electrons only after the surface-confined bipyridinium dications have been reduced. The lack of reversibility indicates that the back oxidation to the bipyridinium dications inhibits the transfer of electrons from the $[Ru(NH_3)_6]^{2+}$ to the electrode. Thus the electroactive multilayer allows the flow of electrons in one direction only in analogy to conventional diodes.

The current/voltage behavior of individual nanoparticles in Fig. 2.16b can be probed by scanning tunneling spectroscopy in an aqueous electrolyte under an inert atmosphere [2.51]. The platinum-iridium tip of a scanning tunneling microscope is positioned above one of the gold particles. The voltage of the gold substrate relative to the tip is maintained at -0.2 V while that relative to a reference electrode immersed in the same electrolyte is varied to control the redox state of the electroactive units. Indeed, the bipyridinium dications in the molecular layer can be reduced reversibly to a monocationic state. The resulting monocations can be reduced further and, once again, reversibly to a neutral form. Finally, the current flowing from the gold support to the tip of the scanning tunneling microscope is monitored as the tip–particle distance increases. From the distance dependence of the current, inverse length decays of ≈ 16 and 7 nm^{-1} for the dicationic and monocationic states, respectively, of the molecular spacer can be determined. The dramatic decrease indicates that the reduction of the electroactive unit facilitates the tunneling of electrons through the gold/molecule/nanoparticle/tip junction. In summary, a change in the redox state of the bipyridinium components can be exploited to gate reversibly the current flowing through this nanoscaled device.

Similar nanostructured materials, combining molecular and nanoparticles layers, can be prepared on layers on indium-tin oxide electrodes following multistep procedures [2.52]. The hydroxylated surfaces of indium-tin oxide supports can be functionalized with 3-ammoniumpropylsilyl groups and then exposed to

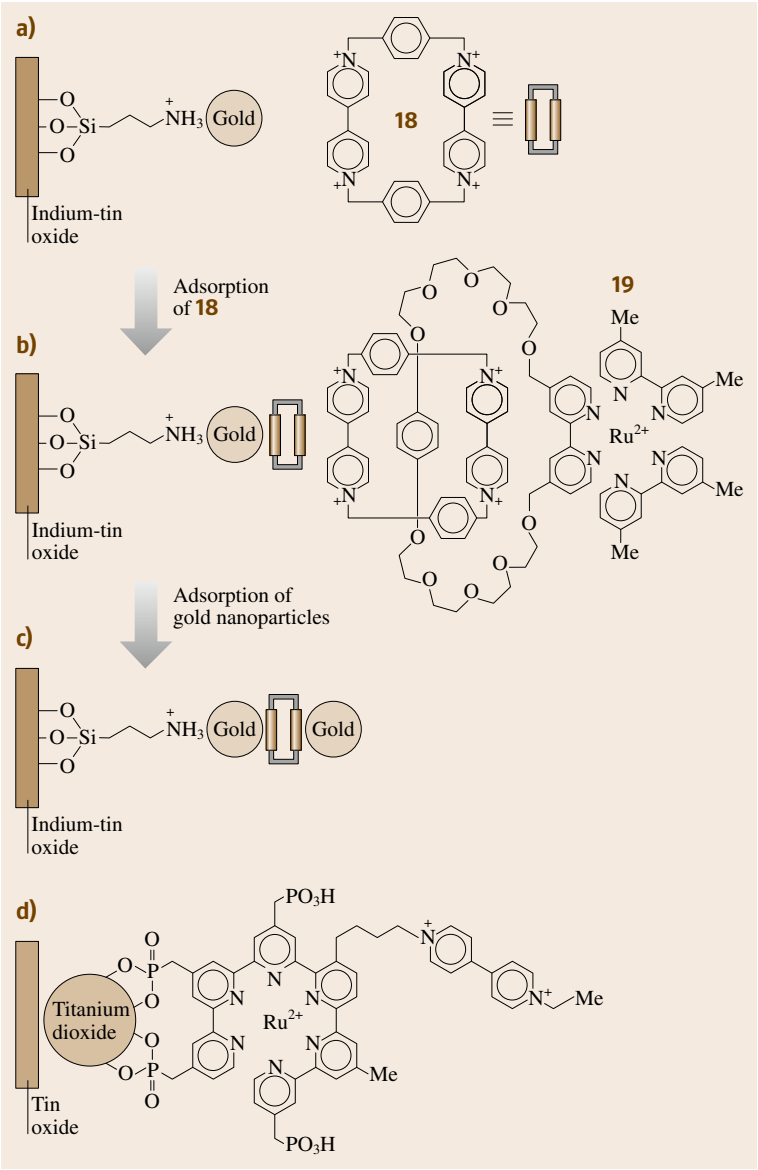

Fig. 2.17 **(a)** Gold nanoparticles assemble spontaneously on pre-functionalized indium-tin oxide electrodes. **(b)** Electrostatic interactions encourage the adsorption of the tetracationic cyclophane **17** on the surface-confined nanoparticles. **(c)** An additional layer of nanoparticles assembles on the cationic organic coating. Similar composite films can be prepared using the tetracationic [2]catenane **18** instead of the cyclophane **17**. **(d)** Phosphonate groups can be used to anchor molecular building blocks to titanium dioxide nanoparticles

gold nanoparticles having a diameter of ≈ 13 nm [2.53, 54]. Electrostatic interactions promote the adsorption of the nanoparticles on the organic layer (Fig. 2.17a). The treatment of the composite film with the bipyridinium cyclophane **17** produces an organic layer on the gold nanoparticles (Fig. 2.18b). Following this approach, alternating layers of inorganic nanoparticles and organic building blocks can be assembled on the indium-tin oxide support. Cyclic voltammograms of the resulting materials show the oxidation of the gold nanoparticles and the reduction of the bipyridinium units. The peak current for both processes increases with the number of alternating layers. Comparison of these values indicates that the ratio between the number of tetracationic cyclophanes and that of the nanoparticles is ≈ 100 : 1.

The tetracationic cyclophane **17** binds dioxyarenes in solution [2.55, 56]. Attractive supramolecular forces between the electron deficient bipyridinium units and the electron rich guests are responsible for complexation. This recognition motif can be exploited to probe

the ability of the composite films in Fig. 2.17b,c to sense electron rich analytes. In particular, hydroquinone is expected to enter the electron deficient cavities of the surface-confined cyclophanes. Cyclic voltammograms consistently reveal the redox waves associated with the reversible oxidation of hydroquinone even when very small amounts of the guest ($\approx 1 \times 10^{-5}$ M) are added to the electrolyte solution [2.53, 54]. No redox response can be detected with a bare indium-tin oxide electrode under otherwise identical conditions. The supramolecular association of the guest and the surface confined cyclophanes increases the local concentration of hydroquinone at the electrode/solution interface enabling its electrochemical detection.

Following a related strategy, the [2]catenane **18** (Fig. 2.17) can be incorporated into similar composite arrays [2.57, 58]. This interlocked molecule incorporates a Ru(II)/trisbipyridine sensitizer and two bipyridinium acceptors. Upon irradiation of the composite material at 440 nm, photoinduced electron transfer from the sensitizer to the appended acceptors occurs. The photogenerated hole in the sensitizer is filled after the transfer of an electron from a sacrificial electron donor present in the electrolyte solution. Under a positive voltage bias applied to the supporting electrode, an electron flow from the bipyridinium acceptors to the indium-tin oxide support is established. The resulting current switches between high and low values as the light source is turned on and off.

Another photoresponsive device, assembled combining inorganic nanoparticles with molecular building blocks, is illustrated in Fig. 2.17d. Phosphonate groups can be used to anchor a Ru(II)/trisbipyridine complex with an appended bipyridinium dication to titanium dioxide nanoparticles deposited on a doped tin oxide electrode [2.59, 60]. The resulting composite array can be integrated in a conventional electrochemical cell filled with an aqueous electrolyte containing triethanolamine. Under a bias voltage of -0.45 V and irradiation at 532 nm, 95% of the excited ruthenium centers transfer electrons to the titanium dioxide nanoparticles. The other 5% donate electrons to the bipyridinium dications. All the electrons transferred to the bipyridinium acceptors return to the ruthenium centers, while only 80% of those accepted by the nanoparticles return to the transition metal complexes. The remaining 15% reach the bipyridinium acceptors, while electron transfer from sacrificial triethanolamine donors fills the photogenerated holes left in the ruthenium sensitizers. The photoinduced reduction of the bipyridinium dication is accompanied by the appearance of the characteristic band of the radical cation in the absorption spectrum. This band persists for hours under open circuit conditions. But it fades in ≈ 15 s under a voltage bias of $+1$ V, as the radical cation is oxidized back to the dicationic form. In summary, an optical stimulation accompanied by a negative voltage bias reduces the bipyridinium building block. The state of the photogenerated form can be read optically, recording the absorption spectrum in the visible region, and erased electrically, applying a positive voltage pulse.

2.3.4 Nanogaps and Nanowires

The operating principles of the electroactive and photoactive devices illustrated in Figs. 2.12–2.17 exploit the ability of small collections of molecular components to manipulate electrons and photons. Designed molecules are deposited on relatively large electrodes and can be addressed electrically and/or optically by controlling the voltage of the support and/or illuminating its surface. The transition from devices relying on collections of molecules to unimolecular devices requires the identification of practical methods to contact single molecules. This fascinating objective demands the rather challenging miniaturization of contacting electrodes to the nanoscale.

A promising approach to unimolecular devices relies on the fabrication of nanometer-sized gaps in metallic features followed by the insertion of individual molecules between the terminals of the gap. This strategy permits the assembly of nanoscaled three-terminal devices equivalent to conventional transistors [2.61–63]. A remarkable example is illustrated in Fig. 2.18a [2.61]. It incorporates a single molecule in the nanogap generated between two gold electrodes. Initially electron beam lithography is used to pattern a gold wire on a doped silicon wafer covered by an insulating silicon dioxide layer. Then the gold feature is broken by electromigration to generate the nanogap. The lateral size of the separated electrodes is ≈ 100 nm and their thickness is ≈ 15 nm. Scanning electron microcopy indicates that the facing surfaces of the separated electrodes are not uniform and that tiny gaps between their protrusions are formed. Current/voltage measurements suggest that the size of the smallest nanogap is ≈ 1 nm. When the breakage of the gold feature is preceded by the deposition of a dilute toluene solution of C_{60} (**19**), junctions with enhanced conduction are obtained. This particular molecule has a diameter of ≈ 0.7 nm and can insert in the nanogap facilitating the flow of electrons across the junction.

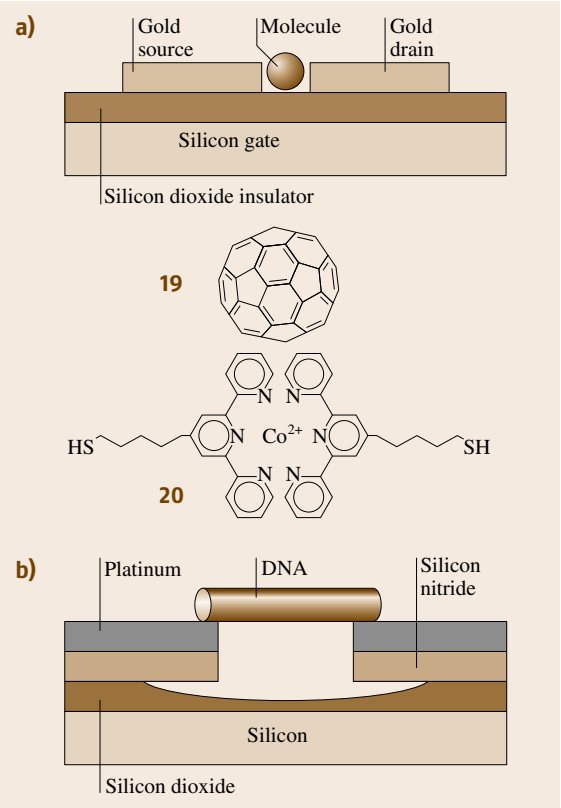

Fig. 2.18 **(a)** Nanoscaled transistors can be fabricated inserting a single molecule (**19** or **20**) between source and drain electrodes mounted on a silicon/silicon dioxide support. **(b)** A DNA nanowire can bridge nanoelectrodes suspended above a silicon dioxide support

The unique configuration of the molecule-based device in Fig. 2.18a can reproduce the functions of a conventional transistor [2.19] at the nanoscale. The two gold terminals of the junction are the drain and source of this nanotransistor, and the underlying silicon wafer is the gate. At a temperature of 1.5 K, the junction conductance is very small, when the gate bias is low, and increases in steps at higher voltages [2.61]. The conductance gap is a consequence of the finite energy required to oxidize/reduce the single C_{60} positioned in the junction. It is interesting that the zero-conductance window also changes with the gate voltage and can be opened and closed reversibly adjusting the gate bias.

A similar strategy can be employed to fabricate a nanoscaled transistor incorporating the Co(II) complex **20** shown in Fig. 2.18 [2.63]. In this instance, a silicon dioxide layer with a thickness of ≈ 30 nm is grown thermally on a doped silicon substrate. Then a gold wire with a width of ≈ 200 nm and a thicknesses of ≈ 10–15 nm is patterned on the silicon dioxide overlayer by electron beam lithography. After extensive washing of the substrate with acetone and methylene chloride and cleaning with oxygen plasma, the gold wire is exposed to a solution of the bisthiol **20**. The formation of thiolate–gold bonds promotes the self-assembly of the molecular building block on the gold surface. At this point, electromigration-induced breakage produces a gap of 1–2 nm in the gold wire. The surface-confined bisthiol **20** is only 0.24 nm long and, therefore, it can insert in the nanogap producing an electrode/molecule/electrode junction.

The cobalt center in **20** can be oxidized/reduced reversibly between Co(II) and Co(III) [2.63]. When this electroactive molecule is inserted in a nanogap (Fig. 2.18a), its ability to accept and donate electrons dictates the current/voltage profile of the resulting electrode/molecule/electrode junction. More precisely, no current flows across the junction below a certain voltage threshold. As the source voltage is raised above this particular value, the drain current increases in steps. The threshold associated with the source voltage varies in magnitude with the gate voltage. This intriguing behavior is a consequence of the finite energy necessary to oxidize/reduce the cobalt center and of a change in the relative stabilities of the oxidized and reduced forms Co(II) and Co(III) with the gate voltage. In summary, the conduction of the electrode/molecule/electrode junction can be tuned adjusting the voltage of the silicon support. The behavior of this molecule-based nanoelectronic device is equivalent to that of a conventional transistor [2.19]. In both instances, the gate voltage regulates the current flowing from the source to the drain.

The electromigration-induced breakage of preformed metallic features successfully produces nanogaps by moving apart two fragments of the same wire. Alternatively, nanogaps can be fabricated reducing the separation of the two terminals of much larger gaps. For example, gold electrodes separated by a distance of 20–80 nm can be patterned on a silicon/silicon dioxide substrate by electron beam lithography [2.64]. The relatively large gap between them can be reduced significantly by the electrochemical deposition of gold on the surfaces of both electrodes. The final result is the fabrication of two nanoelectrodes separated by ≈ 1 nm and with a radius of curvature of 5–15 nm. The two terminals of this nanogap can be *contacted* by organic nanowires grown between them [2.65]. In particular, the

electropolymerization of aniline produces polyaniline bridges between the gold nanoelectrodes. The conductance of the resulting junction can be probed immersing the overall assembly in an electrolyte solution. Employing a bipotentiostat, the bias voltage of the two terminals of the junction can be maintained at 20 mV, while their potentials are scanned relative to that of a silver/silver chloride reference electrode. Below ≈ 0.15 V, the polymer wire is in an insulating state and the current flowing across the junction is less than 0.05 nA. At this voltage threshold, however, the current raises abruptly to ≈ 30 nA. This value corresponds to a conductivity for the polymer nanojunction of $10-100\ \mathrm{S\,cm^{-1}}$. When the potential is lowered again below the threshold, the current returns back to very low values. The abrupt decrease in current in the backward scan is observed at a potential that is slightly more negative than that causing the abrupt current increase in the forward scan. In summary, the conductance of this nanoscaled junction switches on and off as a potential input is switched above and below a voltage threshold.

It is interesting to note that the influence of organic bridges on the junction conductance can be exploited for chemical sensing. Nanogaps fabricated following a similar strategy but lacking the polyaniline bridge alter their conduction after exposure to dilute solutions of small organic molecules [2.66]. Indeed, the organic analytes dock into the nanogaps producing a marked decrease in the junction conductance. The magnitude of the conductance drop happens to be proportional to the analyte–nanoelectrode binding strength. Thus the presence of the analyte in solution can be detected probing the current/voltage characteristics of the nanogaps.

Nanogaps between electrodes patterned on silicon/silicon dioxide supports can be bridged also by DNA double strands [2.67,68]. The device in Fig. 2.18b has a 10.4 nm long poly(G)–poly(C) DNA oligomer suspended between two nanoelectrodes. It can be fabricated patterning a 30 nm wide slit in a silicon nitride overlayer covering a silicon/silicon dioxide support by electron beam evaporation. Underetching the silicon dioxide layer leaves a silicon nitride finger, which can be sputtered with a platinum layer and chopped to leave a nanogap of 8 nm. At this point, a microdroplet of a dilute solution of DNA is deposited on the device and a bias of 5 V is applied between the two electrodes. Electrostatic forces encourage the deposition of a single DNA wire on top of the nanogap. As soon as the nanowire is in position, current starts to flow across the junction. The current/voltage signature of the electrode/DNA/electrode junction shows currents below 1 pA at low voltage biases. Under these conditions, the DNA nanowire is an insulator. Above a certain voltage threshold, however, the nanowire becomes conducting and currents up to 100 nA can flow across the junction through a single nanowire. Assuming that direct tunneling from electrode to electrode is extremely unlikely for a relatively large gap of 8 nm, the intriguing current/voltage behavior has to be a consequence of the participation of the molecular states in the electron transport process. Two possible mechanisms can be envisaged. Sequential hopping of the electrons between states localized in the DNA base pairs can allow the current flow above a certain voltage threshold. But this mechanism would presumably result in a Coulomb blockade voltage gap that is not observed experimentally. More likely, electronic states delocalized across the entire length of the DNA nanowire are producing a molecular conduction band. The off-set between the molecular conduction band and the Fermi levels of the electrodes is responsible for the insulating behavior at low biases. Above a certain voltage threshold, the molecular band and one of the Fermi levels align facilitating the passage of electrons across the junction.

Carbon nanotubes are extremely versatile building blocks for the assembly of nanoscaled electronic devices. They can be used to bridge nanogaps [2.69–72] and assemble nanoscaled cross junctions [2.73–75]. In Fig. 2.19a, a single-wall carbon nanotube crosses over another one in an orthogonal arrangement [2.73]. Both nanotubes have electrical contacts at their ends. The fabrication of this device involves three main steps. First, alignment marks for the electrodes are patterned on a silicon/silicon dioxide support by electron beam lithography. Then the substrate is exposed to a dichloromethane suspension of single-wall SWNT carbon nanotubes. After washing with isopropanol, crosses of carbon nanotubes in an appropriate alignment relative to the electrode marks are identified by tapping mode atomic force microscopy. Finally chromium/gold electrodes are fabricated on top of the nanotube ends, again, by electron beam lithography. The conductance of individual nanotubes can be probed by exploiting the two electric contacts at their ends. These two-terminal measurements reveal that certain nanotubes have metallic behavior, while others are semiconducting. It follows that three distinct types of cross junctions differing in the nature of their constituent nanotubes can be identified on the silicon/silicon dioxide support. Four terminal current/voltage measurements indicate that junctions formed by two metallic nanotubes have high conductance and ohmic behavior.

Similarly, high junction conductance and ohmic behavior is observed when two semiconducting nanotubes cross. The current/voltage signature of junctions formed when a metallic nanotube crosses a semiconducting one are, instead, completely different. The metallic nanotube depletes the semiconducting one at the junction region producing a nanoscaled Schottky barrier with a pronounced rectifying behavior.

Similar fabrication strategies can be exploited to assemble nanoscaled counterparts of conventional transistors. The device in Fig. 2.19b is assembled patterning an aluminum finger on a silicon/silicon dioxide substrate by electron beam lithography [2.75]. After exposure to air, an insulating aluminum oxide layer forms on the aluminum finger. Then a dichloromethane suspension of single-wall carbon nanotubes is deposited on the resulting substrate. Atomic force microscopy can be used to select carbon nanotubes with a diameter of ≈ 1 nm positioned on the aluminum finger. After registering their coordinates relative to alignment markers, gold contacts can be evaporated on their ends by electron beam lithography. The final assembly is a nanoscaled three-terminal device equivalent to a conventional field effect transistor [2.19]. The two gold contacts are the source and drain terminals, while the underlying aluminum finger reproduces the function of the gate. At a source to drain bias of ≈ -1.3 V, the drain current jumps from ≈ 0 to ≈ 50 nA when the gate voltage is lowered from -1.0 to -1.3 V. Thus moderate changes in the gate voltage vary significantly the current flowing through the nanotube-based device in analogy to a conventional enhancement mode p-type field effect transistor [2.19].

The nanoscaled transistor in Fig. 2.18a has a microscaled silicon gate that extends under the entire chip [2.61, 63]. The configuration in Fig. 2.19b, instead, has nanoscaled aluminum gates for every single carbon nanotube transistor fabricated on the same support [2.75]. It follows that multiple nanoscaled transistors can be fabricated on the same chip and operated independently following this strategy. This unique feature offers the possibility of fabricating nanoscaled digital circuits by interconnecting the terminals of independent nanotube transistors. The examples in Fig. 2.19c,d illustrate the configurations of nanoscaled NOT and NOR gates implemented using one or two nanotube transistors. In Fig. 2.19c, an off-chip bias resistor is connected to the drain terminal of a single transistor while the source is grounded. A voltage input applied to the gate modulates the nanotube conductance altering the voltage output probed at the drain terminal. In particular, a voltage input of -1.5 V lowers the nanotube resistance (26 MΩ) below that of the bias resistor (100 MΩ). As a result, the voltage output drops to 0 V. When the voltage input is raised to 0 V, the nanotube resistance increases above that of the bias resistor and the voltage output becomes -1.5 V. Thus

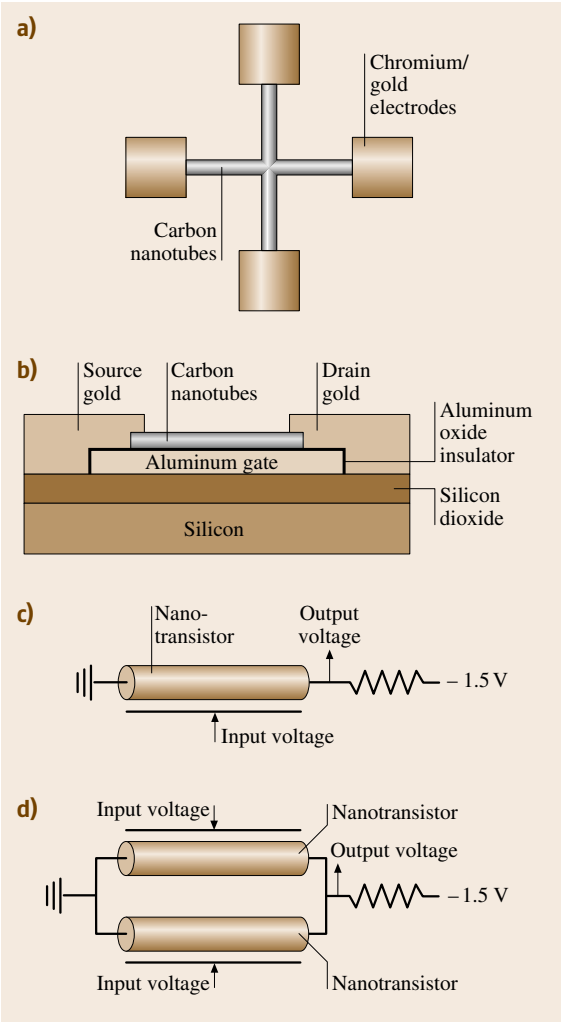

Fig. 2.19 **(a)** Nanoscaled junctions can be assembled on silicon/silicon dioxide supports crossing pairs of orthogonally arranged single-wall carbon nanotubes with chromium/gold electrical contacts at their ends. **(b)** Nanotransistors can be fabricated contacting the two ends of a single-wall carbon nanotube deposited on an aluminum/aluminum oxide gate with gold sources and drain. One or two nanotube transistors can be integrated into nanoscaled NOT **(c)** and NOR **(d)** logic gates

the output of this nanoelectronic device switches from a high (0 V) and to a low (−1.5 V) level as the input shifts from a low (−1.5 V) to a high (0 V) value. The inverse relation between input and output translates into a NOT operation if a negative logic convention (low = 1, high = 0) is applied to both signals.

In Fig. 2.15d, the source terminals of two independent nanotube transistors fabricated on the same chip are connected by a gold wire and grounded [2.75]. Similarly, the two drain terminals are connected by another gold wire and contacted to an off-chip bias resistors. The gate of each nanotube can be stimulated with a voltage input and the voltage output of the device can be probed at their interconnected drain terminals. When the resistance of at least one of the two nanotubes is below that of the resistor, the output is 0 V. When both nanotubes are in a nonconducting mode, the output voltage is −1.5 V. Thus if a low voltage input −1.5 V is applied to one or both transistors, the output is high (0 V). When both voltage inputs are high (0 V), the output is low (−1.5 V). If a negative logic convention (low = 1, high = 0) is applied to all signals, the signal transduction behavior translates in to a NOR operation.

2.4 Conclusions and Outlook

Nature builds nanostructured biomolecules relying on a highly modular approach [2.1]. Small building blocks are connected by robust chemical bonds to generate long strands of repeating units. The synergism of a multitude of attractive supramolecular forces determines the three-dimensional arrangement of the resulting polymeric chains and controls the association of independent strands into single and well-defined entities. Nucleic acids and proteins are two representative classes of biomolecules assembled with subnanometer precision through the subtle interplay of covalent and noncovalent bonds starting from a relatively small pool of nucleotide and amino acid building blocks.

The power of chemical synthesis [2.2] offers the opportunity of mimicking nature's modular approach to nanostructured materials. Following established experimental protocols, small molecular building blocks can be joined together relying on the controlled formation of covalent bonds between designed functional groups. Thus artificial molecules with nanoscaled dimensions can be assembled piece by piece with high structural control. Indeed, helical, tubular, interlocked, and highly branched nanostructures have been all prepared already exploiting this general strategy and the synergism of covalent and noncovalent bonds [2.3].

The chemical construction of nanoscaled molecules from modular building blocks also offers the opportunity for engineering specific properties in the resulting assemblies. In particular, electroactive and photoactive fragments can be integrated into single molecules. The ability of these functional subunits to accept/donate electrons and photons can be exploited to design nanoscaled electronic and photonic devices. Indeed, molecules that respond to electrical and optical stimulations producing detectable outputs have been designed already [2.16]. These chemical systems can be employed to control the interplay of input and output signals at the molecular level. Their conceptual analogy with the signal transduction operated by conventional logic gates in digital circuits is evident. In fact, electroactive and photoactive molecules able to reproduce AND, NOT, and OR operations as well as simple combinational of these basic logic functions are already a reality [2.13, 20, 21].

Most of the molecular switches for digital processing developed so far rely on bulk addressing. In general, relatively large collections of functional molecules are addressed simultaneously in solution. The realization of molecule-based devices with reduced dimensions as well as practical limitations associated with liquid phases in potential applications are encouraging a transition from the solution to the solid state. The general strategy followed so far relies on the deposition of functional molecules on the surfaces of appropriate electrodes following either the Langmuir–Blodgett methodology [2.34] or self-assembly processes [2.35]. The combination of these techniques with the nanofabrication of insulating, metallic, and semiconducting features on appropriate supports has already allowed the realization of fascinating molecule-based devices [2.30–33, 52]. The resulting assemblies integrate inorganic and organic components and, in some instances, even biomolecules to execute specific functions. They can convert optical stimulations into electrical signals. They can execute irreversible and reversible switching operations. They can sense qualitatively and quantitatively specific analytes. They can reproduce the functions of conventional rectifiers and transistors. They can be

integrated within functioning nanoelectronic devices capable of simple logic operations.

The remarkable examples of molecule-based materials and devices now available demonstrate the great potential and promise for this research area. At this stage, the only limit left to the design of functional molecules is the imagination of the synthetic chemist. All sort of molecular building blocks with tailored dimensions, shapes, and properties are more or less accessible with the assistance of modern chemical synthesis. Now, the major challenges are (1) to master the operating principles of the molecule-based devices that have been and continue to be assembled and (2) to expand and improve the fabrication strategies available to incorporate molecules into reliable device architectures. As we continue to gather further insights in these directions, design criteria for a wide diversity of molecule-based devices will emerge. It is not unrealistic to foresee the evolution of an entire generation of nanoscaled devices, based on engineered molecular components, that will find applications in a variety of fields ranging from biomedical research to information technology. Perhaps nature can once again illuminate our path, teaching us not only how to synthesize nanostructured molecules but also how to use them. After all, nature is replete with examples of extremely sophisticated molecule-based devices. From tiny bacteria to higher animals, we are all a collection of molecule-based devices.

References

2.1 D. Voet, J.G. Voet: *Biochemistry* (Wiley, New York 1995)

2.2 K.C. Nicolau, E.C. Sorensen: *Classics in Total Synthesis* (VCH, Weinheim 1996)

2.3 J.-M. Lehn: *Supramolecular Chemistry: Concepts and Perspectives* (VCH, Weinheim 1995)

2.4 M.M. Harding, U. Koert, J.-M. Lehn, A. Marquis-Rigault, C. Piguet, J. Siegel: Synthesis of unsubstituted and 4,4′-substituted oligobipyridines as ligand strands for helicate self-assembly, Helv. Chim. Acta **74**, 594–610 (1991)

2.5 J.-M. Lehn, A. Rigault, J. Siegel, B. Harrowfield, B. Chevrier, D. Moras: Spontaneous assembly of double-stranded helicates from oligobipyridine ligands and copper(I) cations: Structure of an inorganic double helix, Proc. Natl. Acad. Sci. USA **84**, 2565–2569 (1987)

2.6 J.-M. Lehn, A. Rigault: Helicates: Tetra- and pentanuclear double helix complexes of Cu(I) and poly(bipyridine) strands, Angew. Chem. Int. Ed. Engl. **27**, 1095–1097 (1988)

2.7 J.D. Hartgerink, J.R. Granja, R.A. Milligan, M.R. Ghadiri: Self-assembling peptide nanotubes, J. Am. Chem. Soc. **118**, 43–50 (1996)

2.8 M.R. Ghadiri, J.R. Granja, R.A. Milligan, D.E. McRee, N. Khazanovich: Self-assembling organic nanotubes based on a cyclic peptide architecture, Nature **366**, 324–327 (1993)

2.9 V. Balzani, A. Credi, F.M. Raymo, J.F. Stoddart: Artificial molecular machines, Angew. Chem. Int. Ed. **39**, 3348–3391 (2000)

2.10 A.J. Bard, L.R. Faulkner: *Electrochemical Methods: Fundamentals and Applications* (Wiley, New York 2000)

2.11 V. Balzani (Ed.): *Electron Transfer in Chemistry* (Wiley-VCH, Weinheim 2001)

2.12 J.D. Coyle: *Principles and Applications of Photochemistry* (Wiley, New York 1988)

2.13 V. Balzani, M. Venturi, A. Credi: *Molecular Devices and Machines* (Wiley-VCH, Weinheim 2003)

2.14 P.R. Ashton, R. Ballardini, V. Balzani, A. Credi, K.R. Dress, E. Ishow, C.J. Kleverlaan, O. Kocian, J.A. Preece, N. Spencer, J.F. Stoddart, M. Venturi, S. Wenger: A photochemically driven molecular-level abacus, Chem. Eur. J. **6**, 3558–3574 (2000)

2.15 M. Irié (Ed.): Photochromism: memories and switches, Chem. Rev. **100**, 1683–1890 (2000)

2.16 B.L. Feringa (Ed.): *Molecular Switches* (Wiley-VCH, Weinheim 2001)

2.17 R.J. Mitchell: *Microprocessor Systems: An Introduction* (Macmillan, London 1995)

2.18 D.R. Smith: *Digital Transmission Systems* (Van Nostrand Reinhold, New York 1993)

2.19 S. Madhu: *Electronics: Circuits and Systems* (SAMS, Indianapolis 1985)

2.20 F.M. Raymo: Digital processing and communication with molecular switches, Adv. Mater. **14**, 401–414 (2002)

2.21 A.P. de Silva: Molecular computation – Molecular logic gets loaded, Nat. Mater. **4**, 15–16 (2005)

2.22 A. Aviram: Molecules for memory, logic and amplification, J. Am. Chem. Soc. **110**, 5687–5692 (1988)

2.23 A.P. de Silva, H.Q.N. Gunaratne, C.P. McCoy: A molecular photoionic AND gate based on fluorescent signaling, Nature **364**, 42–44 (1993)

2.24 M. Asakawa, P.R. Ashton, V. Balzani, A. Credi, G. Mattersteig, O.A. Matthews, M. Montalti, N. Spencer, J.F. Stoddart, M. Venturi: Electrochemically induced molecular motions in pseudorotaxanes: A case of dual-mode (oxidative and reductive) dethreading, Chem. Eur. J. **3**, 1992–1996 (1997)

2.25 F.M. Raymo, S. Giordani, A.J.P. White, D.J. Williams: Digital processing with a three-state molecular switch, J. Org. Chem. **68**, 4158–4169 (2003)

2.26 F.M. Raymo, S. Giordani: Signal communication between molecular switches, Org. Lett. **3**, 3475–3478 (2001)

2.27 F.M. Raymo, S. Giordani: Multichannel digital transmission in an optical network of communicating molecules, J. Am. Chem. Soc. **124**, 2004–2007 (2002)

2.28 F.M. Raymo, S. Giordani: All-optical processing with molecular switches, Proc. Natl. Acad. Sci. USA **99**, 4941–4944 (2002)

2.29 A.J. Bard: *Integrated Chemical Systems: A Chemical Approach to Nanotechnology* (Wiley, New York 1994)

2.30 C. Joachim, J.K. Gimzewski, A. Aviram: Electronics using hybrid-molecular and mono-molecular devices, Nature **408**, 541–548 (2000)

2.31 J.M. Tour: Molecular electronics. Synthesis and testing of components, Acc. Chem. Res. **33**, 791–804 (2000)

2.32 A.R. Pease, J.O. Jeppesen, J.F. Stoddart, Y. Luo, C.P. Collier, J.R. Heath: Switching devices based on interlocked molecules, Acc. Chem. Res. **34**, 433–444 (2001)

2.33 R.M. Metzger: Unimolecular electrical rectifiers, Chem. Rev. **103**, 3803–3834 (2003)

2.34 M.C. Petty: *Langmuir–Blodgett Films: An Introduction* (Cambridge Univ. Press, Cambridge 1996)

2.35 A. Ulman: *An Introduction to Ultrathin Organic Films* (Academic, Boston 1991)

2.36 C. Lee, A.J. Bard: Comparative electrochemical studies of *N*-methyl-*N*′-hexadecyl viologen monomolecular films formed by irreversible adsorption and the Langmuir–Blodgett method, J. Electroanal. Chem. **239**, 441–446 (1988)

2.37 C. Lee, A.J. Bard: Cyclic voltammetry and Langmuir film isotherms of mixed monolayers of *N*-docosoyl-*N*′-methyl viologen with arachidic acid, Chem. Phys. Lett. **170**, 57–60 (1990)

2.38 M. Fujihira, K. Nishiyama, H. Yamada: Photoelectrochemical responses of optically transparent electrodes modified with Langmuir–Blodgett films consisting of surfactant derivatives of electron donor, acceptor and sensitizer molecules, Thin Solid Films **132**, 77–82 (1985)

2.39 M. Fujihira: Photoelectric conversion with Langmuir–Blodgett films. In: *Nanostructures Based on Molecular Materials*, ed. by W. Göpel, C. Ziegler (VCH, Weinheim 1992) pp. 27–46

2.40 C.P. Collier, E.W. Wong, M. Belohradsky, F.M. Raymo, J.F. Stoddart, P.J. Kuekes, R.S. Williams, J.R. Heath: Electronically configurable molecular-based logic gates, Science **285**, 391–394 (1999)

2.41 E.W. Wong, C.P. Collier, M. Belohradsky, F.M. Raymo, J.F. Stoddart, J.R. Heath: Fabrication and transport properties of single-molecule-thick electrochemical junctions, J. Am. Chem. Soc. **122**, 5831–5840 (2000)

2.42 M. Asakawa, P.R. Ashton, V. Balzani, A. Credi, C. Hamers, G. Mattersteig, M. Montalti, A.N. Shipway, N. Spencer, J.F. Stoddart, M.S. Tolley, M. Venturi, A.J.P. White, D.J. Williams: A chemically and electrochemically switchable [2]catenane incorporating a tetrathiafulvalene unit, Angew. Chem. Int. Ed. **37**, 333–337 (1998)

2.43 V. Balzani, A. Credi, G. Mattersteig, O.A. Matthews, F.M. Raymo, J.F. Stoddart, M. Venturi, A.J.P. White, D.J. Williams: Switching of pseudorotaxanes and catenanes incorporating a tetrathiafulvalene unit by redox and chemical inputs, J. Org. Chem. **65**, 1924–1936 (2000)

2.44 M. Asakawa, M. Higuchi, G. Mattersteig, T. Nakamura, A.R. Pease, F.M. Raymo, T. Shimizu, J.F. Stoddart: Current/voltage characteristics of monolayers of redox-switchable [2]catenanes on gold, Adv. Mater. **12**, 1099–1102 (2000)

2.45 C.P. Collier, G. Mattersteig, E.W. Wong, Y. Luo, K. Beverly, J. Sampaio, F.M. Raymo, J.F. Stoddart, J.R. Heath: A [2]catenane based solid-state electronically reconfigurable switch, Science **289**, 1172–1175 (2000)

2.46 C.P. Collier, J.O. Jeppesen, Y. Luo, J. Perkins, E.W. Wong, J.R. Heath, J.F. Stoddart: Molecular-based electronically switchable tunnel junction devices, J. Am. Chem. Soc. **123**, 12632–12641 (2001)

2.47 J. Chen, M.A. Reed, A.M. Rawlett, J.M. Tour: Large on-off ratios and negative differential resistance in a molecular electronic device, Science **286**, 1550–1552 (1999)

2.48 M.A. Reed, J. Chen, A.M. Rawlett, D.W. Price, J.M. Tour: Molecular random access memory cell, Appl. Phys. Lett. **78**, 3735–3737 (2001)

2.49 D.I. Gittins, D. Bethell, R.J. Nichols, D.J. Schiffrin: Redox-controlled multilayers of discrete gold particles: A novel electroactive nanomaterial, Adv. Mater. **9**, 737–740 (1999)

2.50 D.I. Gittins, D. Bethell, R.J. Nichols, D.J. Schiffrin: Diode-like electron transfer across nanostructured films containing a redox ligand, J. Mater. Chem. **10**, 79–83 (2000)

2.51 D.I. Gittins, D. Bethell, D.J. Schiffrin, R.J. Nichols: A nanometer-scale electronic switch consisting of a metal cluster and redox-addressable groups, Nature **408**, 67–69 (2000)

2.52 A.N. Shipway, M. Lahav, I. Willner: Nanostructured gold colloid electrodes, Adv. Mater. **12**, 993–998 (2000)

2.53 A.N. Shipway, M. Lahav, R. Blonder, I. Willner: Bis-bipyridinium cyclophane receptor–Au nanoparticle superstructure for electrochemical sensing applications, Chem. Mater. **11**, 13–15 (1999)

2.54 M. Lahav, A.N. Shipway, I. Willner, M.B. Nielsen, J.F. Stoddart: An enlarged bis-bipyridinum cyclophane–Au nanoparticle superstructure for selective electrochemical sensing applications, J. Electroanal. Chem. **482**, 217–221 (2000)

2.55 R.E. Gillard, F.M. Raymo, J.F. Stoddart: Controlling self-assembly, Chem. Eur. J. **3**, 1933–1940 (1997)

2.56 F.M. Raymo, J.F. Stoddart: From supramolecular complexes to interlocked molecular compounds, Chemtracts Org. Chem. **11**, 491–511 (1998)

2.57 M. Lahav, T. Gabriel, A.N. Shipway, I. Willner: Assembly of a Zn(II)-porphyrin-bipyridinium dyad and Au-nanoparticle superstructures on conductive surfaces, J. Am. Chem. Soc. **121**, 258–259 (1999)

2.58 M. Lahav, V. Heleg-Shabtai, J. Wasserman, E. Katz, I. Willner, H. Durr, Y. Hu, S.H. Bossmann: Photoelectrochemistry with integrated photosensitizer-electron acceptor Au-nanoparticle arrays, J. Am. Chem. Soc. **122**, 11480–11487 (2000)

2.59 G. Will, S.N. Rao, D. Fitzmaurice: Heterosupramolecular optical write-read-erase device, J. Mater. Chem. **9**, 2297–2299 (1999)

2.60 A. Merrins, C. Kleverlann, G. Will, S.N. Rao, F. Scandola, D. Fitzmaurice: Time-resolved optical spectroscopy of heterosupramolecular assemblies based on nanostructured TiO_2 films modified by chemisorption of covalently linked ruthenium and viologen complex components, J. Phys. Chem. B **105**, 2998–3004 (2001)

2.61 H. Park, J. Park, A.K.L. Lim, E.H. Anderson, A.P. Alivisatos, P.L. McEuen: Nanomechanical oscillations in a single C_{60} transistor, Nature **407**, 57–60 (2000)

2.62 W. Liang, M.P. Shores, M. Bockrath, J.R. Long, H. Park: Kondo resonance in a single-molecule transistor, Nature **417**, 725–729 (2002)

2.63 J. Park, A.N. Pasupathy, J.I. Goldsmith, C. Chang, Y. Yaish, J.R. Petta, M. Rinkoski, J.P. Sethna, H.D. Abruna, P.L. McEuen, D.C. Ralph: Coulomb blockade and the Kondo effect in single-atom transistors, Nature **417**, 722–725 (2002)

2.64 C.Z. Li, H.X. He, N.J. Tao: Quantized tunneling current in the metallic nanogaps formed by electrodeposition and etching, Appl. Phys. Lett. **77**, 3995–3997 (2000)

2.65 H. He, J. Zhu, N.J. Tao, L.A. Nagahara, I. Amlani, R. Tsui: A conducting polymer nanojunction switch, J. Am. Chem. Soc. **123**, 7730–7731 (2001)

2.66 A. Bogozi, O. Lam, H. He, C. Li, N.J. Tao, L.A. Nagahara, I. Amlani, R. Tsui: Molecular adsorption onto metallic quantum wires, J. Am. Chem. Soc. **123**, 4585–4590 (2001)

2.67 A. Bezryadin, C.N. Lau, M. Tinkham: Quantum suppression of superconductivity in ultrathin nanowires, Nature **404**, 971–974 (2000)

2.68 D. Porath, A. Bezryadin, S. de Vries, C. Dekker: Direct measurement of electrical transport through DNA molecules, Nature **403**, 635–638 (2000)

2.69 S.J. Tans, M.H. Devoret, H. Dai, A. Thess, E.E. Smalley, L.J. Geerligs, C. Dekker: Individual single-wall carbon nanotubes as quantum wires, Nature **386**, 474–477 (1997)

2.70 A.F. Morpurgo, J. Kong, C.M. Marcus, H. Dai: Gate-controlled superconducting proximity effect in carbon nanotubes, Nature **286**, 263–265 (1999)

2.71 J. Nygård, D.H. Cobden, P.E. Lindelof: Kondo physics in carbon nanotubes, Nature **408**, 342–346 (2000)

2.72 W. Liang, M. Bockrath, D. Bozovic, J.H. Hafner, M. Tinkham, H. Park: Fabry–Perot interference in a nanotube electron waveguide, Nature **411**, 665–669 (2001)

2.73 M.S. Fuhrer, J. Nygård, L. Shih, M. Forero, Y.-G. Yoon, M.S.C. Mazzoni, H.J. Choi, J. Ihm, S.G. Louie, A. Zettl, P.L. McEuen: Crossed nanotube junctions, Science **288**, 494–497 (2000)

2.74 T. Rueckes, K. Kim, E. Joselevich, G.Y. Tseng, C.-L. Cheung, C.M. Lieber: Carbon nanotube-based nonvolatile random access memory for molecular computing, Science **289**, 94–97 (2000)

2.75 A. Bachtold, P. Hadley, T. Nakanishi, C. Dekker: Logic circuits with carbon nanotube transistors, Science **294**, 1317–1320 (2001)